12-1995

Compressible Turbulence Measurement in the Mixing Layer of an Adiabatic Normal Slot Injection into Supersonic Flow

Christopher D. Whitcomb

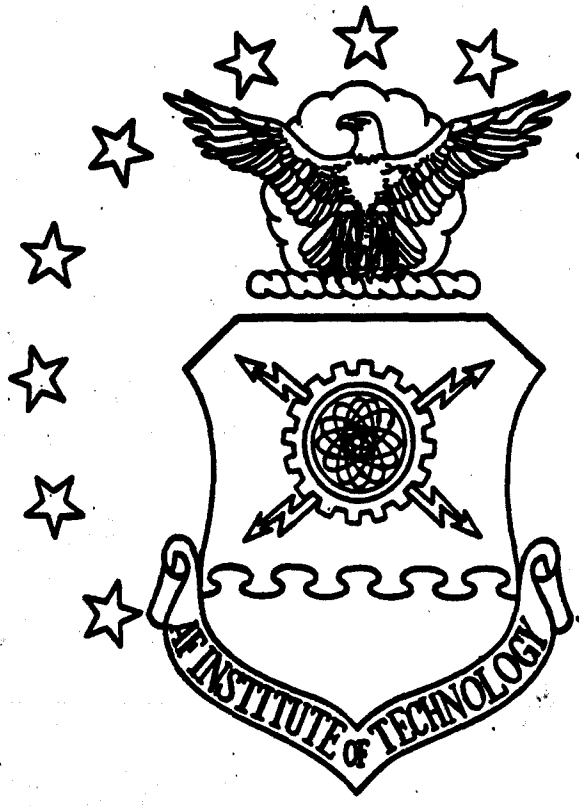

COMPRESSIBLE TURBULENCE MEASUREMENT IN THE MIXING LAYER OF AN ADIABATIC NORMAL SLOT INJECTION INTO SUPERSONIC FLOW

THESIS
Christopher Duane Whitcomb
Captain, USAF

AFIT/GAE/ENY/95D

DEPARTMENT OF THE AIR FORCE
AIR UNIVERSITY
AIR FORCE INSTITUTE OF TECHNOLOGY

Wright-Patterson Air Force Base, Ohio

AFIT/GAE/ENY/95D-24

COMPRESSIBLE TURBULENCE MEASUREMENT IN THE MIXING LAYER OF AN ADIABATIC NORMAL SLOT INJECTION INTO SUPERSONIC FLOW

THESIS
Christopher Duane Whitcomb
Captain, USAF

AFIT/GAE/ENY/95D

Approved for public release; distribution unlimited

The views expressed in this thesis are those of the author and do not reflect the official policy or position of the Department of Defense or the U.S. Government.

AFIT/GAE/ENY/95D-24

COMPRESSIBLE TURBULENCE MEASUREMENT IN THE MIXING LAYER OF AN ADIABATIC NORMAL SLOT INJECTION INTO SUPERSONIC FLOW

THESIS

Presented to the Faculty of the Graduate School of Engineering
of the Air Force Institute of Technology
Air University
In Partial Fulfillment of the
Requirements for the Degree of
Master of Science in Aeronautical Engineering

Christopher Duane Whitcomb, B.S.
Captain, USAF

December 1995

Acknowledgments

The first and most important person that I want to thank is my wife, Cindy. Without her undying patience, love, and understanding, this accomplishment would not have been possible. I would also to thank my wonderful daughter for understanding that daddy couldn't play most of the time.

The next person I want to thank is my thesis advisor, Dr. Rodney Bowersox. His enthusiasm, continual support of this project, and extensive knowledge of the subject kept me going when things were not necessarily going as planned.

Lastly, I would like to thank my fellow students that had to put up with my many questions, especially 2nd Lt Colin Tucker. Without their help and knowledge, this work would not have been completed on time.

Table of Contents

Page

List of Figures

List of Tables

List of Symbols

a,b	Hot-wire calibration constants
f,g	Hot-wire sensitivities
k	Thermal conductivity
M	Mach number
Nu	Nusselt number
P, p	Pressure
Pr	Prandtl number
q	Heat flux
Re	Reynolds Number
T	Temperature
u, v, w	Velocity components
W	Injector throat width
x, y, z	Cartesian coordinates
α, β	Hot-wire functions of Mach number
γ	Ratio of specific heats
μ	Viscosity
ρ	Density
τ	Shear stress
ϕ	Hot-wire incidence angle

Subscripts

c	Cone-static
e	Effective
o	Reference Condition
T	Turbulent

t	total
w	wire
∞	infinity

Superscripts

T	Turbulent
$( )'$	Fluctuating component
$\overline{( )}$	Mean component

ABSTRACT

In this study mean flow and compressible turbulence measurements were taken at a station x = 72W downstream of the injection, where W is the injector throat width, of an adiabatic 2-D Mach 1.6 normal slot injection into a Mach 2.9 flow. Data were collected using a conventional Pitot probe, a cone-static probe, and multiple overheat cross-wire anemometry. In addition, schlieren and shadowgraph flow visualization was used to investigate the flow structure at both the injection point and at the downstream data collection point. From these measurements, mass flux component turbulence intensities of 8% to 10% were seen. The total temperature fluctuation was shown to be 6%, which was higher than expected for this adiabatic case. It was also determined that the incompressible component of the Reynolds shear stress accounted for 75% of the total Reynolds shear stress. Another important observation was that the density fluctuation turbulence intensity peaked near the freestream edge of the mixing layer. The turbulent dissipation of kinetic energy was most likely the cause of this peak.

COMPRESSIBLE TURBULENCE MEASUREMENT IN THE MIXING LAYER OF AN ADIABATIC NORMAL SLOT INJECTION INTO SUPERSONIC FLOW

I. Introduction

1.1 Objective and Motivation

The overall objective for the present study is to provide data in the turbulent mixing layer of an adiabatic 2-D supersonic injection into a supersonic cross-flow that will enhance the understanding of the associated flow physics, aid the validation of computational fluid dynamics (CFD) codes, and improve compressible turbulence modeling. Since essentially all high speed flows of practical interest are turbulent, the understanding of the flow conditions in a turbulent flow are essential to the solution of many current aerospace endeavors. One such endeavor is the supersonic combustion ramjet (SCRAMjet) engine for the National Aerospace Plane (NASP). Other relevant studies include thrust vector regulation systems of rocket motors and reaction control jets of high-speed flight vehicles.[1] SCRAMjet engines require fuel be injected into a supersonic flow, mixed rapidly, and then combusted. The expense and difficulty of running such an engine require that accurate computer models of the engine and the flow physics associated with it be developed to optimize the SCRAMjet's design. One way to develop these models is to build mockups of the engine and test them in wind tunnels, but since this

is time consuming, expensive, and for some conditions not feasible, the emphasis has been directed toward computational methods. Currently these techniques are hindered by inaccurate turbulence models that do not fully consider the compressible turbulent phenomenon. The development and validation of these models have been thwarted by the extreme scarcity of data.

1.2 Requirement for Turbulence Modeling

Turbulent flows are governed by the full unsteady Navier-Stokes equations. The difficulty with this is that the current and next generation computers have neither the speed nor storage capacity necessary to fully solve the unsteady Navier-Stokes equations for practical flow problems. This problem arises because of the fact that turbulent flows are characterized by a range of time and length scales that vary over several orders of magnitude. Based on current trends in the computer resources, it will probably be well into the next century before computers posses the speed and memory requirements necessary to calculate turbulent flow properties from the unsteady Navier-Stokes equations.[2] Hence engineers must currently rely on approximate methods to provide acceptable solutions to turbulent flows. These approximate methods admittedly do not account for all of the physics of turbulent flow.

The two most used approximations include the Reynolds-averaged (time-averaged) Navier-Stokes equations (RANS) and the Favre-averaged (or mass-averaged) Navier-Stokes equations (FANS). Both of these methods require some type of closure formulation because they produce more unknowns than

equations. Turbulence modeling is the process by which the number of unknowns is reduced to the number of equations.

The development of these turbulence models relies heavily on experimental data and physical intuition. The lack of compressible turbulence data has lead to direct extensions of incompressible models and ad-hoc assumptions.[3] Overall, these extensions and assumptions have been shown to be questionable for compressible flows.[4] The expense and difficulty of measuring the compressible components of turbulence have impeded the generation of experimental data. It is also necessary to use experimental methods which can measure the necessary compressible terms in the Navier-Stokes equations and report the data in a form which is applicable to both theoretical and computational efforts. Bowersox[5] addressed these issues as will this study. Lastly, in order for turbulence measurements to be useful to the turbulence modeler, they must be of sufficient quality to validate CFD codes. This means the geometries must be simple enough so that they can be modeled without difficulty.[3]

1.3 Flowfield

The flowfield used in this study is shown in Figure 1.1. As can be seen from this figure, the flowfield created by a normal supersonic injection in a supersonic cross-flow has associated with it, very violent and complex physics. As shown in the figure, the turbulent boundary layer is disturbed causing a separation bubble and shock to occur. Behind the shock, the injection plume continues to expanded outside the nozzle and produce a jet induced shock that the rest of the flowfield must pass through. The injection plume then

decelerates and encounters a normal shock, call a Mach disk, to achieve pressure equilibrium within the flow. The supersonic cross-flow expands and accelerates as it flows over the jet. Downstream of the injection, the two fluid streams begin mixing. The flow then encounters a recompression shock to turn the flow parallel to the wall. The mixing region is much larger than the upstream turbulent boundary layer, and continues to grow after encountering the recompression shock. The measurements taken in this study were taken downstream of this recompression shock at a position of x = 72W (where W = the width of the injector throat). A more detailed description of the flowfield is given in Chapter 5.

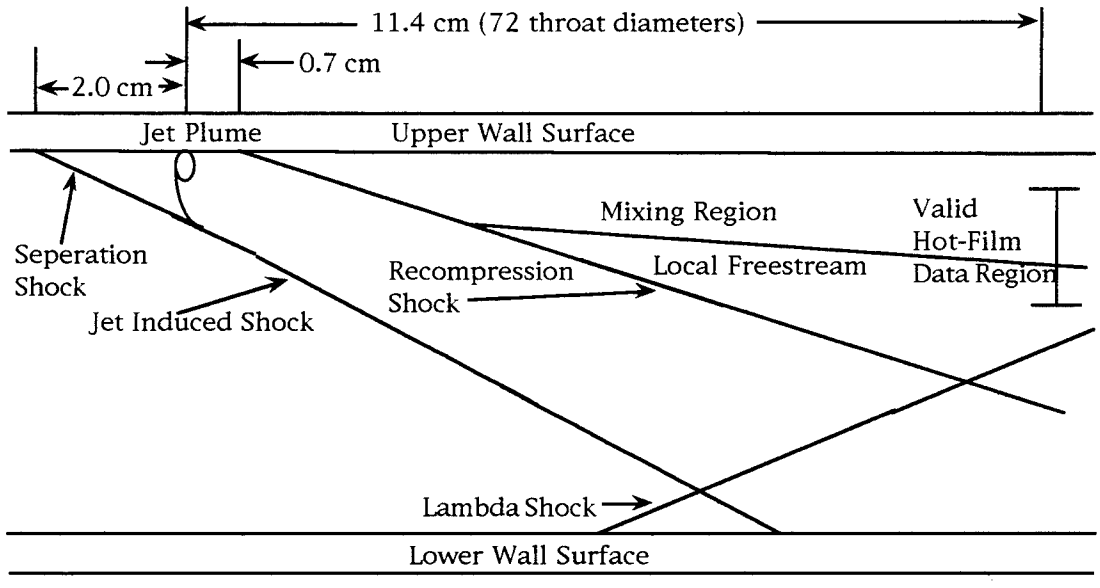

Figure 1.1: Sketch of the Flowfield[6]

1.4 Scope of Present Study

This study aims to expand the current understanding of mixing and turbulence associated with a supersonic normal slot injection is injected into a

supersonic flow. This was done by first examining the governing equation of the turbulent flow physics described in Chapter 2. Next an injector model was designed based on the necessary flow parameters, and Mach number contour plots were produced at two x locations to ensure the two dimentionality of the flowfield. The next step was to take the necessary data. Chapter 3 describes the injection model that was used in the study as well as the facilities and instrumentation used to take the data in this study. The last step was to reduce the data and determine the results of the study. Chapter 4 steps through the data reduction of the mean and multiple overheat cross-wire data that was collected. Chapter 5 describes the results of the shadowgraph and schlieren photograph, the mean flow probe data, and the cross-flow data. And lastly Chapter 6 presents the conclusion of the study and makes some recommendations for further study.

II. Equation Development

This chapter develops the averaged forms of the unsteady Navier-Stokes equations relative to the present work. As mentioned in Chapter 1, the two most common forms of the unsteady Navier-Stokes equations are the Reynolds (time)-averaged (RANS) and the Favre (mass-weighted)-averaged (FANS) Navier-Stokes equations.

2.1 Compressible Navier-Stokes Equations

The full unsteady, compressible Navier-Stokes equations[2] are presented below because they are needed in the development of the RANS and FANS equations.

$$\text{continuity: } \frac{\partial \rho}{\partial t} + \frac{\partial}{\partial x_j}\left(\rho u_j\right) = 0 \tag{2.1}$$

$$\text{momentum: } \frac{\partial}{\partial t}\left(\rho u_i\right) + \frac{\partial}{\partial x_j}\left(\rho u_i u_i\right) = -\frac{\partial P}{\partial x_i} + \frac{\partial}{\partial x_j}\left(\tau_{ij}\right) \tag{2.2}$$

$$\text{energy: } \frac{\partial}{\partial t}\left(\rho h_o\right) + \frac{\partial}{\partial x_j}\left(\rho u_j h_o\right) = \frac{\partial P}{\partial t} + \frac{\partial}{\partial x_j}\left(u\tau_{ij} - q_j\right) \tag{2.3}$$

Numerical solutions to the equations given above for high Reynolds number turbulent flows are not available at this time, thus approximate methods must be utilized. Time averaging the equations leads to the RANS equations.

2.2 *Reynolds-Averaged Navier-Stokes (RANS) Equations*

This section presents the results of Reynolds averaging applied to the conservative form of the governing equations. The standard way of dealing with turbulent flows is to separate the instantaneous flow properties into a mean component and a fluctuating component. The instantaneous flow properties become:

$$\begin{aligned} u_i &= \overline{u_i} + u_i' & h_o &= \overline{h_o} + h_o' \\ P &= \overline{P} + P' & q_i &= \overline{q_i} + q_i' \\ \rho &= \overline{\rho} + \rho' & \tau_{ij} &= \overline{\tau_{ij}} + \tau_{ij}' \end{aligned} \tag{2.4}$$

The barred quantities are time averaged over a period longer than the longest fluctuation but shorter than any unsteadiness of the mean flow. The prime quantities are the deviations from the average.[7] Next the flow variables are time averaged according to

$$\overline{u} = \int_0^{t_o-T} u(x,y,z,t)dt \tag{2.5}$$

By substituting the mean and fluctuating components of Equation (2.4) into the governing Equations (2.1) - (2.3) and employing the time averaging of Equation (2.5), the Reynolds-averaged Navier-Stokes (RANS) equations are obtained. These equations are given in Equations (2.6) through (2.8).

$$\text{continuity: } \frac{\partial \bar{\rho}}{\partial t} + \frac{\partial}{\partial x_j}\left(\bar{\rho}\bar{u}_j + \overline{\rho' u_j'}\right) = 0 \tag{2.6}$$

$$\text{momentum: } \frac{\partial}{\partial t}\left(\bar{\rho}\bar{u}_i + \overline{\rho' u_i'}\right) + \frac{\partial}{\partial x_j}\left(\bar{\rho}\bar{u}_i\bar{u}_j\right) = -\frac{\partial \bar{p}}{\partial x_i} + \frac{\partial}{\partial x_j}\left(\tau_{ij} + \tau_{ij}^T\right) \tag{2.7}$$

$$\text{energy: } \frac{\partial}{\partial t}\left(\bar{\rho}\bar{e}_o + \overline{\rho' h_o'}\right) + \frac{\partial}{\partial x_j}\left(\bar{\rho}\bar{h}_o\bar{u}_j\right) = \frac{\partial}{\partial x_j}\left(\bar{u}_i\bar{\tau}_{ij} + \overline{u_i'\tau_{ij}'} - q_j - q_j^T\right) \tag{2.8}$$

In the above equations, the laminar shear and heat flux terms are given by

$$\tau_{ij} = \mu\left(\frac{\partial u_i}{\partial x_j} + \frac{\partial u_j}{\partial x_i}\right) \tag{2.9}$$

$$\tau_{ii} = 2\mu\frac{\partial u_i}{\partial x_i} - \frac{2}{3}\mu\nabla \bullet \bar{V} \tag{2.10}$$

$$q_i = -k\frac{\partial T}{\partial x_i} \tag{2.11}$$

and the turbulent shear and heat flux terms are given by

$$\tau_{ij}^T = -\bar{\rho}\overline{u_i'u_j'} - \bar{u}_i\overline{\rho' u_j'} - \bar{u}_j\overline{\rho' u_i'} - \overline{\rho' u_i' u_j'} \tag{2.12}$$

$$q_i^T = \bar{\rho}\overline{h_o' u_i'} - \bar{h}_o\overline{\rho' u_i'} - \bar{u}_i\overline{\rho' h_o'} - \overline{\rho' h_o' u_i'} \tag{2.13}$$

It should be noted that the averaging process eliminates the turbulent flow frequency, phase, and wavelength.

In incompressible flow, the last three terms of both Equations (2.12) and (2.13) are identically zero. In compressible flows, the last term of both Equations (2.12) and (2.13) is a triple correlation and therefore is assumed to be small and is generally ignored. The second and third terms are significant, and their exclusion in incompressible extensions to compressible flows has led to the failure of such extensions to fully model the physics of compressible turbulence.

2.3 Favre-Averaged Navier-Stokes (FANS) Equations

Favre-averaging (mass-weighted) is the second averaging method used on the Navier-Stokes equations. A complete derivation of the Favre-averaged Navier-Stokes equations can be found in Wilcox.[8] The FANS also eliminate some flow information. Like the RANS equations, they eliminate the turbulent flow phase, frequency, and wavelength, but they also eliminate the explicit moments of the density fluctuations. The FANS equations have been applied to compressible flows by using extensions of incompressible turbulence models. Favre-averaging methods have had some success in boundary layer flows at moderate Mach number, but they have not performed well in free shear layers, or in the presence of compression and expansion waves.[4] The flow conditions in the present study contain both compression and expansion waves.

2.4 Turbulence Transformation

The right-hand sides of Equations (2.12) and (2.13) must be transformed into experimentally measurable terms. This section presents a method by which these equations are transformed into an equivalent expression that can be measured by multiple overheat cross-wire anemometry. This transformation follows the procedure developed by Bowersox.[9]

The transformation begins with the following identity

$$\rho\phi = \left(\overline{\rho\phi}\right) + \left(\rho\phi\right)' \tag{2.14}$$

$$\rho\phi = \left(\bar{\rho} + \rho'\right)\left(\bar{\phi} + \phi'\right) \tag{2.15}$$

where ϕ is a generic variable. Setting the right-hand sides of Equations (2.14) and (2.15) equal produces

$$\overline{\rho\phi} + \left(\rho\phi\right)' = \left(\overline{\rho} + \rho'\right)\left(\overline{\phi} + \phi'\right) \tag{2.16}$$

Time averaging Equation (2.16) produces

$$\overline{\rho\phi} = \overline{\rho}\overline{\phi} + \overline{\rho'\phi'} \tag{2.17}$$

Subtracting Equation (2.17) from Equation (2.16) yields the fluctuation relation

$$\left(\rho\phi\right)' = \overline{\rho}\phi' + \overline{\phi}\rho' + \left(\rho'\phi' - \overline{\rho'\phi'}\right) \tag{2.18}$$

By substituting $\phi = u_i$ and $\phi = u_j$ into Equation (2.18) and forming the products $(\rho u_i)'$ and $(\rho u_j)'$, the terms in the Reynolds shear, Equation (2.12), can be collected on one side of the equation to produce the Reynolds shear transformation

$$\tau_{ij}^{T} = -\frac{\overline{\left(\rho u_i\right)'\left(\rho u_j\right)'}}{\overline{\rho}} + \overline{\rho}\,\overline{u}_i\overline{u}_j\overline{\left(\frac{\rho'}{\overline{\rho}}\right)^2} \tag{2.19}$$

In this formulation, the triple correlation $\overline{\rho' u_i' u_j'}$ and fourth order terms were neglected. In a similar manner, the Reynolds heat flux terms can be shown to be

$$q_i^{T} = \overline{\left(\rho u_i\right)' h_o'} + \overline{h}_o\overline{\rho' u_i'} \tag{2.20}$$

All the terms that appear in Equations (2.19) and (2.20) can be measured directly or estimated by separation of cross-wire variables. Chapter 4 goes through the details of how the cross-wire data can be reduced.

III Facilities and Instrumentation

This chapter describes the experimental and computational facilities and the instrumentation used in this study. The description includes an overview of the Air Force Institute of Technology (AFIT) Mach 2.9 wind tunnel, the injector model used in the study, the equipment necessary for the flow visual techniques used in the study, and the experimental instrumentation used. Finally a brief description of the computational facilities used is given.

3.1 Supersonic Wind Tunnel

This experimental work was performed in the AFIT Mach 2.9 wind tunnel. A sketch of the wind tunnel layout is shown below in Figure 3.1.

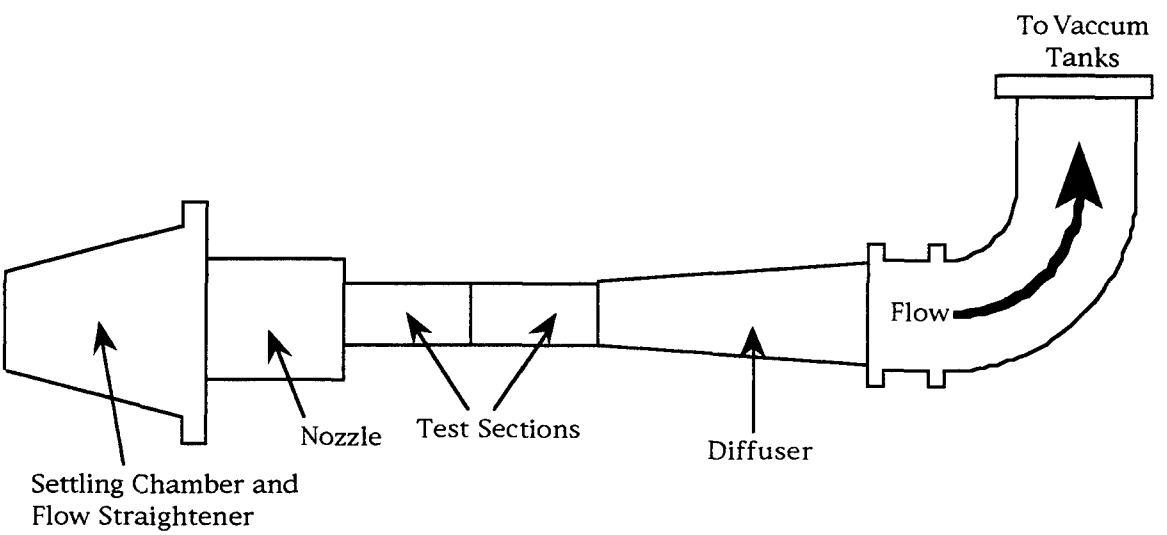

Figure 3.1: Wind Tunnel Layout

The wind tunnel consists of a settling chamber with a flow straightener, a removable Mach 2.9 nozzle, two interchangeable 6.35 cm x 6.35 cm test sections, and a variable diffuser. The flow straightener within the wind tunnel's settling chamber is a multi-screen type flow straightener. The settling chamber also contains a thermocouple and a Pitot probe. Both of these devices are located downstream of the flow straightener just before the convergent portion of the nozzle. This location was chosen to account for any pressure drop encounter across the flow straightener. The Pitot probe in conjunction with an Endevco 0-690 kPag pressure transducer is used to measure the settling chamber stagnation pressure ($P_{t\infty}$). The thermocouple is used to measure the total temperature ($T_{t\infty}$) of the flow and is an Omega Engineering Type K (chromel-alumel) thermocouple constructed of Type 316 stainless steel. The test sections consist of four removable parts; two side walls, a ceiling, and a floor. With this setup, different ceilings or floors can be placed in the tunnel allowing for a robust setup of different experiments. For this study, the floor was flat with two ports drilled into it that allowed for the placement of the conventional and hot-wire probes at x/W = 72. The ceiling was smooth and contained the injector model, the exit of which was flush with the ceiling surface. The two side walls were 1.91 cm thick plexiglass that allowed for ease in probe placement and light source alignment for shadowgraph and schlieren flow visualization. These were later replaced with side walls containing two 5.08 cm diameter circular optical grade glass windows for improved schlieren flow visualization. The tunnel diffuser was optimized to allow for run times of 25-30 seconds. The tunnel operates on a combination of pressure and vacuum.

The pressure side of the tunnel operates on 0.69 MPa air pressure. This is provided by two Atlas Copco GAU 807 compressors at a mass flow rate of 0.5 kg/sec. The air used is dried by two Pioneer Refrigerant Air Dryers before entering the laboratory, and then dried and cleaned again by a cyclone separator and multiple layers of cloth fiber filter paper prior to it entering the wind tunnel.

The vacuum required for operation of the wind tunnel is provided by sixteen storage tanks (volume $\approx 16\ m^3$) which are evacuated by three 7.5 hp, 230 V Stokes Micro Vac pump. These pumps are shown in Figure 3.2 below. These pumps could provide a vacuum of approximately 2 mmHg, but most runs were made at between 10 and 15 mmHg.

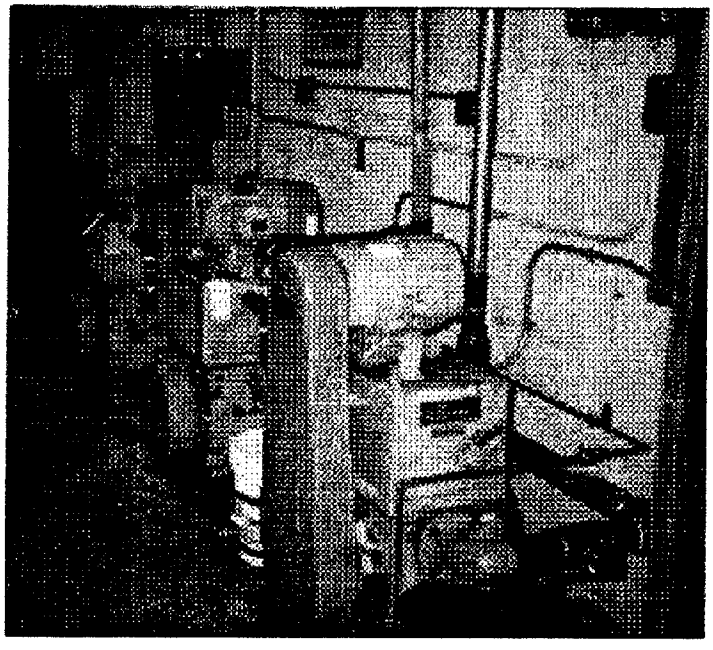

Figure 3.2: The Stokes Micro Vac pumps

The wind tunnel was run manually by opening the valve to the vacuum tanks and then opening the valve to the high pressure supply. The tunnel was turned off by reversing the above procedure. The

3.2 Injector Model

The purpose of this study being to investigate the turbulence within a two dimensional mixing layer of a supersonic injection and a supersonic cross-flow, an injector that could provide this situation had to be designed.

3.2.1 Injector Model Design Considerations. In designing the injector model that was used in this study, several factors were considered. First, the flowfield had to be two dimensional. This was handled by using a slot injection. The two dimensionality of the flow is further discussed in the Chapter 5. The second factor was the fact that the injected flow needed to be supersonic. To accomplish this, a small converging-diverging nozzle was designed to provide an injector Mach number of 1.6. The last factor was ease of construction. This was accomplished by designing the injector nozzle to fit into an existing wind tunnel ceiling.

3.2.2 Injector Model. The injector was designed in two parts, the injector adapter and the injector nozzle. This design is pictured in Figure 3.3.

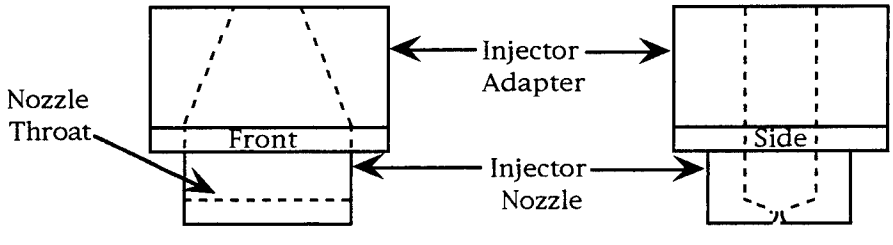

Figure 3.3: Injector Model

The injector nozzle fits into the ceiling of the test section and contains the injector plenum and the converging-diverging nozzle. As mentioned above,

the nozzle was designed to inject into the freestream at Mach 1.6, which required an area ratio of 1.25. The throat was 1.59 mm wide by 4.45 cm long. Based on this throat area, the exit width was determined to be 1.98 mm with the same length. The injector nozzle also contains the lower portion of the injector plenum which is 1.91 cm wide by 4.45 long by 1.27 cm deep after which it converges to the throat dimensions. A schematic of the injector nozzle is shown in Figure 3.4.

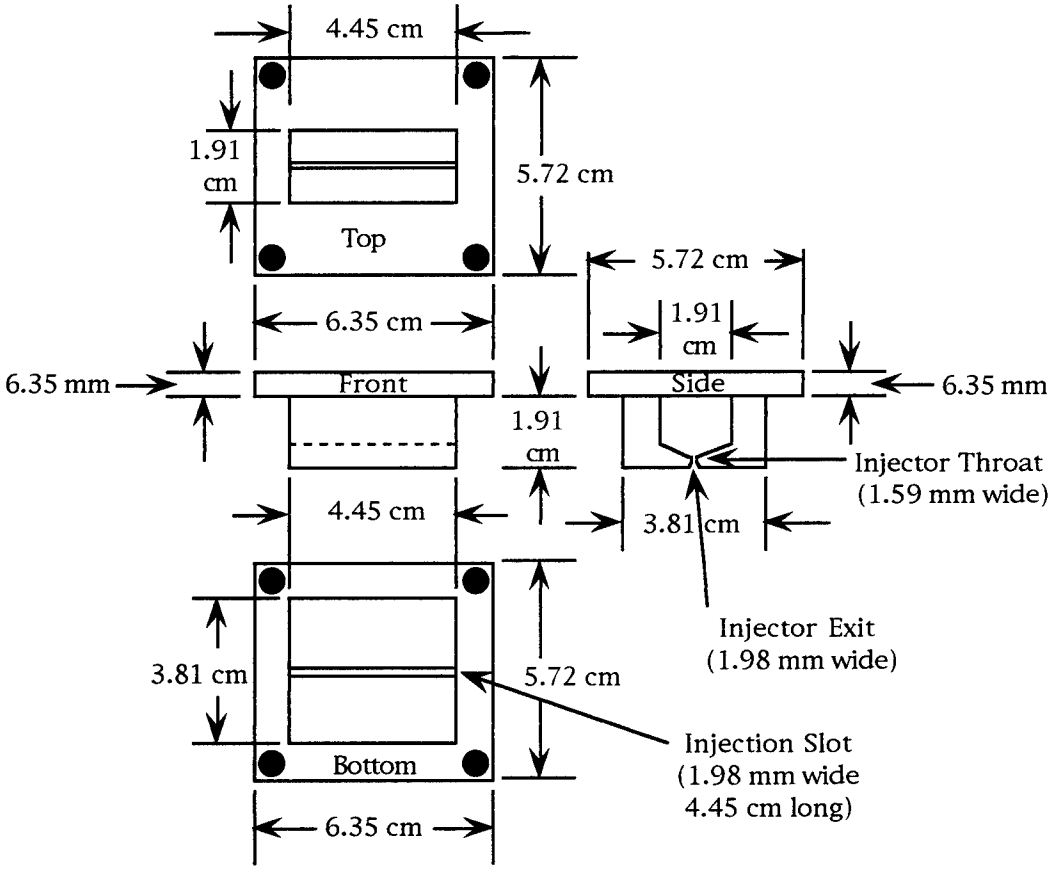

Figure 3.4: Schematic of the Injector Nozzle

The injector adapter fits on top of the injector nozzle and was used to connect the air supply tubing to the injector nozzle. A tap was drilled into the top of the adapter to accept a 1.27 cm (inner diameter) pipe that supplied the

injector's air. This opening was then expanded to match the dimensions of the injector plenum. During the runs, the injector's air supply was bled off the tunnel settling chamber. The bottom of the adapter has an o-ring which ensured a seal between the injector adapter and injector nozzle. The adapter was also tapped to accept a pressure transducer and a thermocouple. An Endevco 0-345 kPag pressure transducer was used in the pressure transducer tap to measure the injector stagnation pressure. An Omega Engineering Type K (chromel-alumel) thermocouple constructed of Type 316 stainless steel was used in the thermocouple tap to measure the injector total temperature. A schematic of the injector adapter is shown in Figure 3.5.

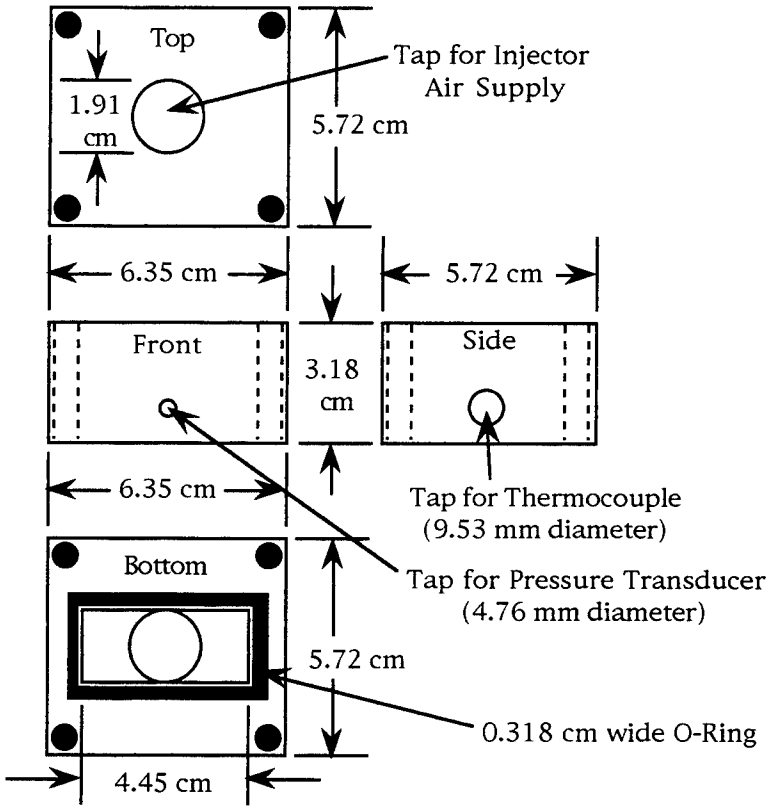

Figure 3.5: Injector Adapter Schematic

The adapter and nozzle are bolted to the test section ceiling such that the injector exit is perpendicular to the test section wall. Sketches of the experimental setup and the coordinate system used in the experiment are shown in Figures 3.6 and 3.7 respectively.

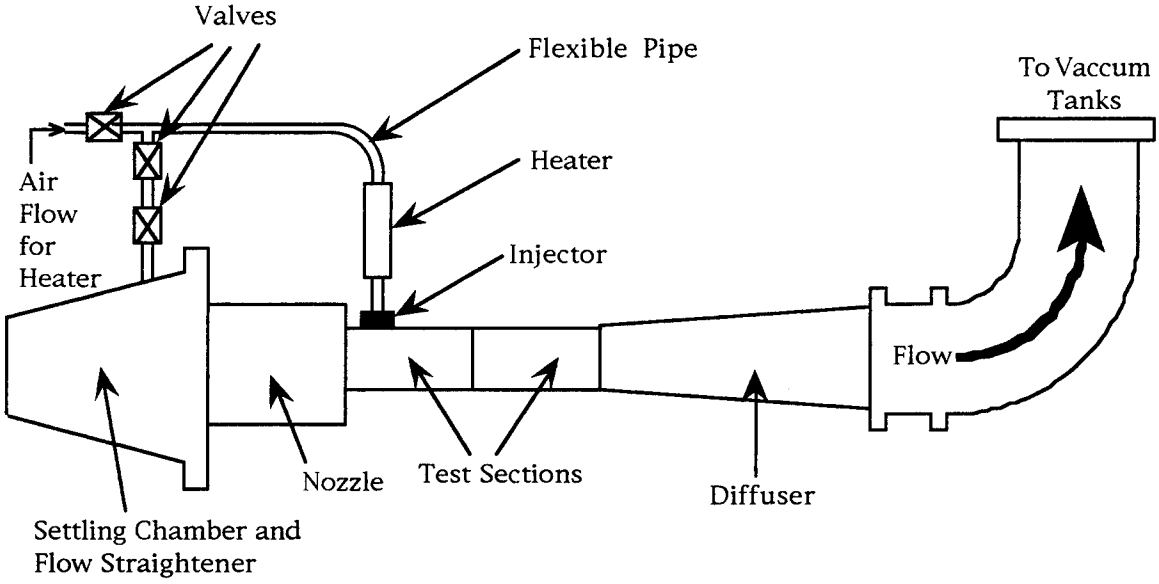

Figure 3.6a: Experimental Setup

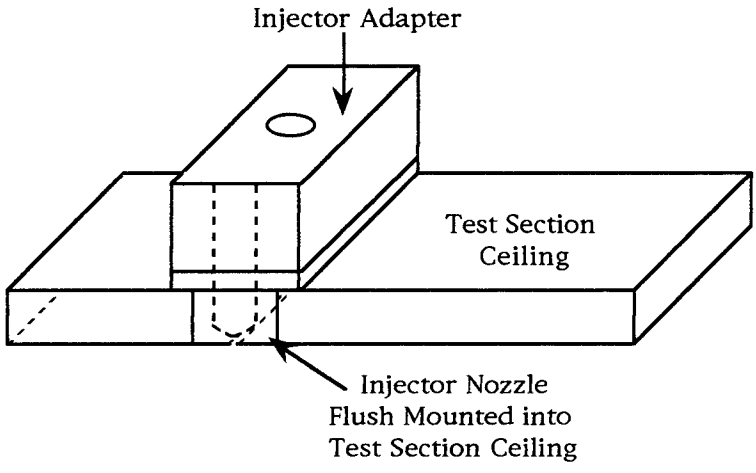

Figure 3.6b: Flush Mounting of Injector Nozzle

The heater shown in Figure 3.6a was included in this setup for use in a companion non-adiabatic injection study. The valve closest to the settling chamber was used to regulate the amount of air that flows through the injector during the runs. The pressure in the injector settling chamber was kept at a constant 69 kPa. The second value was used as an on/off valve.

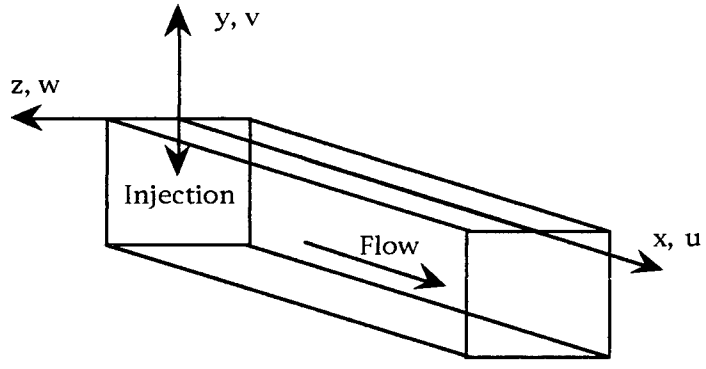

Figure 3.7: Experiment Coordinate System

The flowfield conditions produced in the freestream of the wind tunnel and within the injector are tabulated below in Table 3.1. The relative values between the two are also listed there as well.

Table 3.1: Flowfield Conditions Summary

Freestream	Injector	Relative
$M = 2.9$	$M = 1.6$	$u_{inj}/u_\infty = 0.73$
$P_{t\infty} = 204$ kPa	$P_{t\infty} = 60.7$ kPa	$P_{tinj}/P_{t\infty} = 0.3$
$T_{t\infty} = 298$ K	$T_{t\infty} = 298$	$T_{tinj}/T_{t\infty} = 1.0$
$\dot{m} = 0.5$ kg/s	$\dot{m} = 0.01$ kg/s	$(\rho u)_{inj}/(\rho u)_\infty = 0.92$
		$\rho_{inj}/\rho_\infty = 1.25$

3.3 Flow Visualization

Both 10 nanosecond spark schlieren and shadowgraph photography were used for flow visualization. With the laboratory lights off, the light source was triggered manually after the wind tunnel was started and the film was exposed. The film was then covered back up, the tunnel was turned off, and the film was removed. After twenty to thirty seconds, the photograph was examined. The setup for the flow visualizations is dicussed below.

3.3.1 Shadowgraph Setup. Shadowgraph photographs were taken of the entire flowfield including the injection and the downstream measuring position. The light source used was a Xenon Corporation Novatron 289B Nanopulse lamp, which was powered by a Model-437A Nanopulser. The light was reflected into the test section by a collimating mirror with a 1.524 m focal length. The camera was placed approximately 0.15 m from the test section and used Type 57 Polaroid film. A sketch of the shadowgraph setup is given in Figure 3.8.

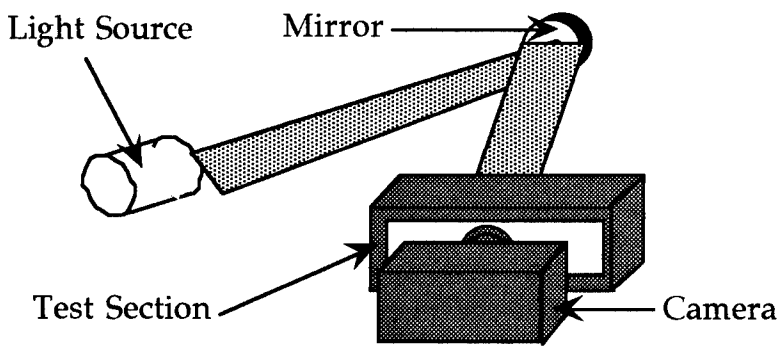

Figure 3.8: Shadowgraph Flow Visualization Setup

3.3.2 Schlieren Setup. Schlieren photographs were also taken of the entire flowfield including the injection and the downstream measuring position. Schlieren photographs were taken with both the plexiglass side

walls and the side walls with the optical grade circular glass windows. The light source used was also the Xenon Corporation Novatron 289B Nanopulse lamp, which was powered by a Model-437A Nanopulser. The light was reflected into the test section by a collimating mirror with a 1.524 m focal length. The light was then reflected to a knife edge by another collimating mirror with a 1.525 m focal length. Placing the knife edge in a vertical position proved to produce the best schlieren results. After the knife edge, the light was reflected through a lens and to the camera by a flat mirror. The camera was placed at the position that produced the most focused image on the opaque screen in the rear of the camera. The film used for the photographs was Type 57 Polaroid film. A sketch of the schlieren setup is given in Figure 3.9.

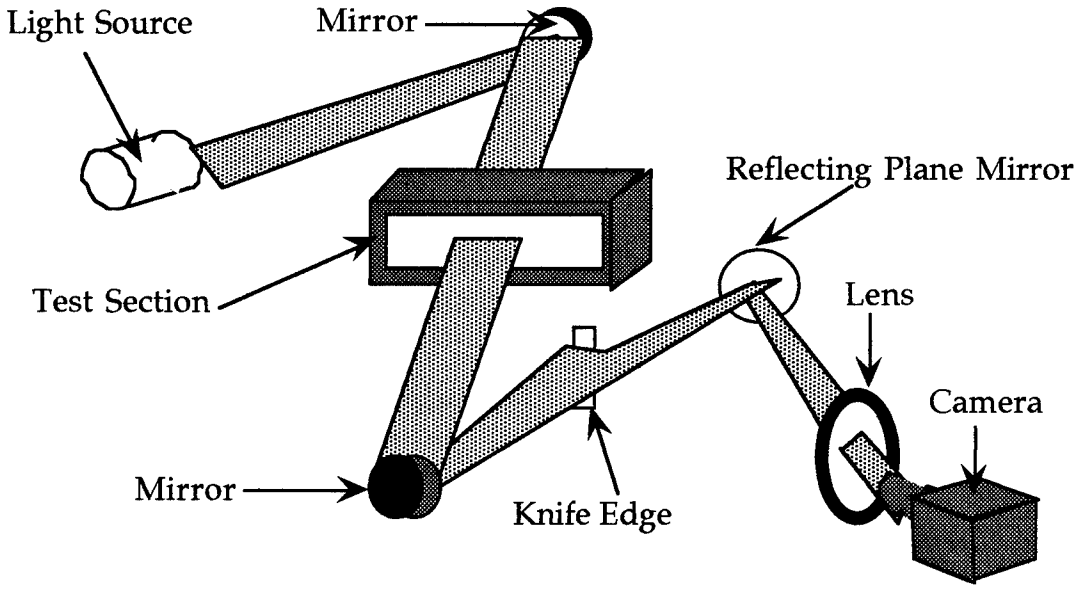

Figure 3.9: Schlieren Flow Visualization Setup

3.4 Mean Flow Instrumentation

3.4.1 Settling Chamber. During the run of the wind tunnel, the total pressure within the settling chamber was held constant at roughly 204 ± 3 kPa. This data was supplied by the Endevco 0-690 kPag pressure transducer and recorded by the Nicolet Data Acquisition System (NDAS) which will be described in section 3.4.3. The pressure transducer signal was used for the trigger of the Nicolet system for the cross-wire (Section 3.5) calibration runs. The pressure was kept constant during the tunnel runs by a mechanical pressure regulation system. This system consists of a Fairchild pneumatic pressure regulator and a Leslie pressure reducing valve. The total temperature was also monitored during each run of the wind tunnel. As mentioned earlier it was sensed by an Omega Engineering thermocouple. This temperature was not recorded by Nicolet during a run of the tunnel, because it did not vary more than ± 1 K. Overall, the temperature was constant at 298 ± 3 K.

3.4.2 Traverse and LVDT System. The position of the probes used to collect the mean flow data was controlled by the traverse and linear voltage displacement transducer (LVDT) system. The traverse consists of an Arrick Robotics MD-2 dual stepper motor driver package and a Size 23 Stepper Motor. The LVDT system is a TransTek Inc. Model 0217 linear voltage displacement transducer.[10] The stepper motor was controlled by a Compaq 386 computer and a BASIC computer program. Each probe was secured in the traverse and then positioned at its starting point. The tunnel was then started and the traverse was triggered using the computer program. With the triggering of the traverse, the probe was moved vertically in the flowfield the amount and direction specified in the program. While the motor was moving, its position was sensed by the LVDT

and the signal was recorded by the Nicolet. The traverse and LVDT system setup is shown in Figure 3.10.

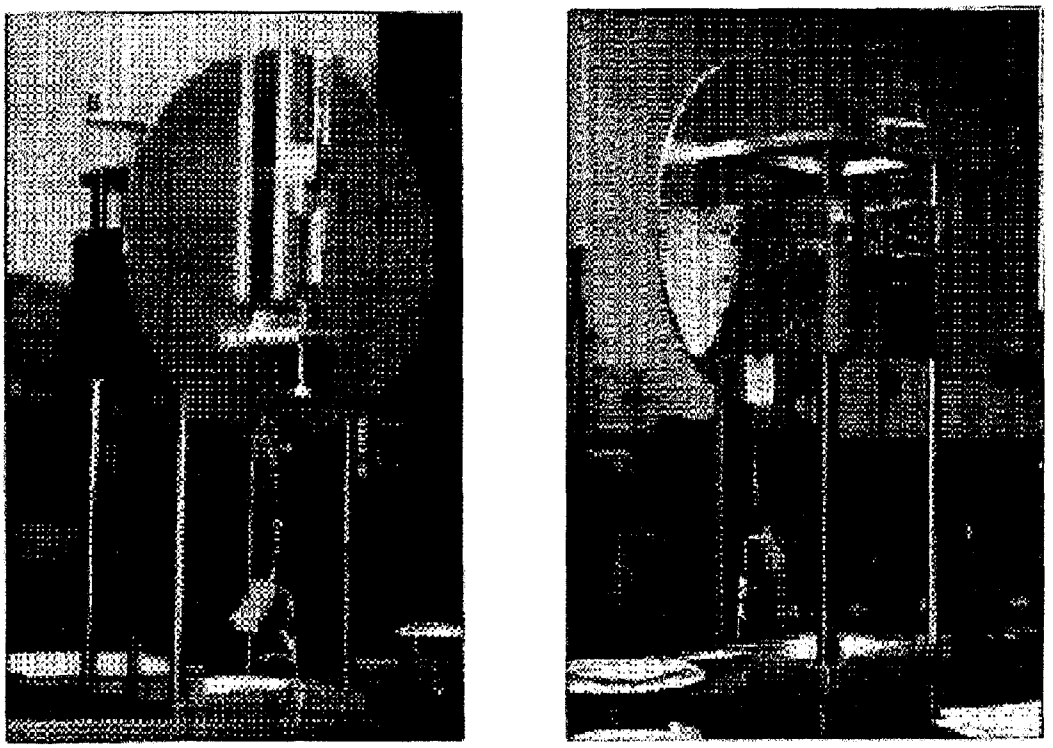

Figure 3.10: Traverse and LVDT System

3.4.3 Nicolet Data Acquisition System. All the data collected during the tunnel runs were transferred to the Nicolet for recording. For the mean flow runs, this data included the settling chamber total pressure, the injector total pressure, the Pitot probe or cone-static pressure, and the probe position via the LVDT. The Nicolet Data Acquisition System consisted of a Nicolet MultiPro 120 Digitizer[11] that contained four cards with 4 channels each. For the mean flow data, four channels were used to record the data from the various sensors. Table 3.1 shows which channels were used for what data. For the mean flow data, the sampling rate was set at 200 Hz, which allowed for a collection period of 26 seconds.

Table 3.2: Mean Flow Data Channels

Nicolet Card	Card Channel	Data Sampled
Card A	Channel 1	settling chamber total pressure
Card B	Channel 1	injector total pressure
Card C	Channel 1	Pitot or cone-static pressure
Card A	Channel 2	probe position

3.4.4 Filters and Signal Conditioners. The mean flow signals from the various sensors were conditioned, filtered, and amplified before being sent to the Nicolet. Signals from the pressure transducers were sent through Endevco Model 4423 Signal Conditioners which supplied excitation voltage to the transducers, filtered the signal, and also amplified the signal. The signal from the LVDT system was passed through a TransTek Model 1000-0012 oscillator/demodulator.

3.4.5 Downstream Pressure Probes. The mean flow data was collected using two different types of probes, a conventional Pitot probe and a 10° half-angle cone-static probe. Both probes are pictured in Figure 3.11.

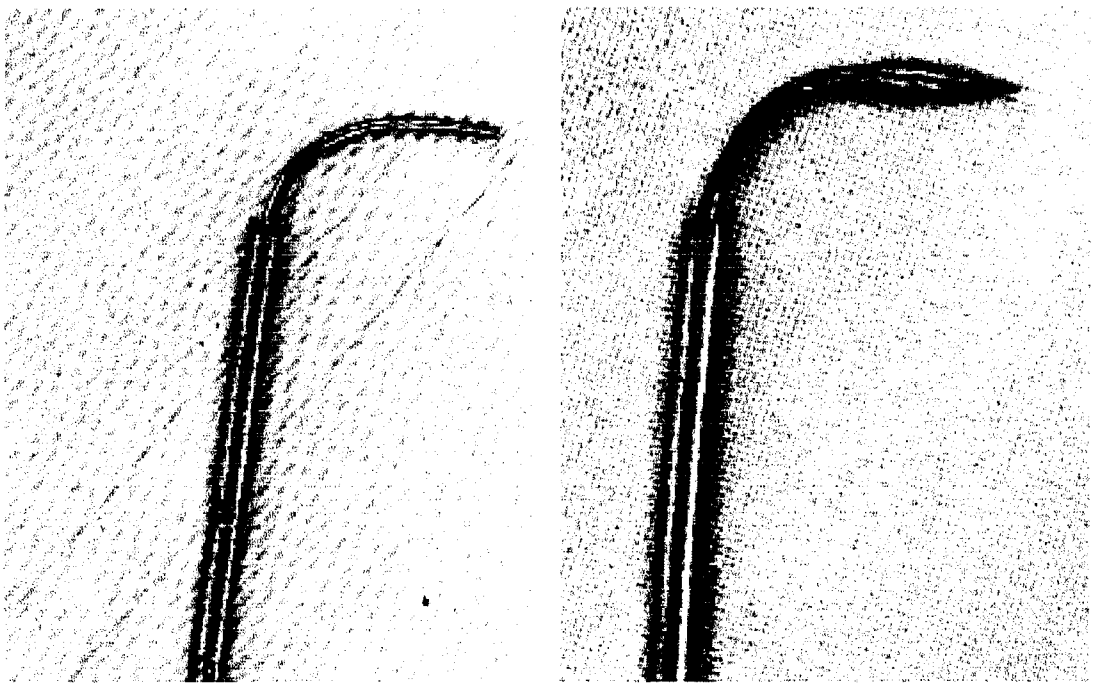

Pitot Probe Cone-Static Probe

Figure 3.11: Pitot and Cone-Static Pressure Probes[12]

The Pitot probe was constructed of a 1.59 mm outer diameter stainless steel tube which was inserted into a 3.18 mm outer diameter stainless steel tube. The outer tube was used for reinforcement of the inner tube. The opening of the Pitot tube was crimped so that the horizontal dimension was twice as large as the vertical dimension. The Pitot probe pressure was sensed by an Endevco 0-103 kPag pressure transducer.

The cone-static probe has a 10° ± 0.03° semi-vertex angle axisymmetric cone machined from stainless steel. The cone tip has four 0.34 mm (#80 drill) pressure taps at 90° intervals around the circumference and 4.3 mm from the tip of the cone. These four pressure taps meet in a common chamber where they are averaged to account for misalignment errors of ± 6.0°- 7.0°.[13] This cone was soldered to 1.59 mm tubing which again was inserted into a 3.18 mm

tube for reinforcement. As with the Pitot probe, the cone-static probe pressure was sensed by an Endevco 0-103 kPag pressure transducer.

3.5 Hot-Wire Instrumentation

The turbulence measurements required a more sophisticated sensing device. Cross-wire hot-wire probes were used to make these measurements. The data acquisition procedure for the hot-wire data was essential the same as that for the mean for, so only the differences will be highlighted here.

3.5.1 Nicolet Data Acquisition System. Once again the Nicolet system was used for data collection. The only difference is that the mean flow Pitot or cone-static pressure channel was replaced by two hot-wire data channels. In order to assure the most accurate representation of the turbulence, more data points had to be collected. To collect the most data points, the sampling rate was set to 20 kHz. This rate allowed for the most data to be collected while still allowing the traverse to travel the distance required, which was 2.03 cm. This sampling rate gave a sampling period of 13 seconds. Table 3.2 shows which channels were used for what data.

Table 3.3: Hot-Wire Data Channels

Nicolet Card	Card Channel	Data Sampled
Card A	Channel 1	settling chamber total pressure
Card A	Channel 2	probe position
Card A	Channel 3	hot-wire wire 1
Card A	Channel 4	hot-wire wire 2
Card B	Channel 1	injector total pressure

3.5.2 Cross-Wire Probe. As mentioned above, a cross-wire hot-wire probe was used to measure the turbulence in the mixing layer. The probe used in this work was a TSI Inc. Model 1243-20 platinum hot film probe.[14] This model of probe acquires the x-y or "uv" turbulence data. A schematic of such a probe is shown below in Figure 3.12.

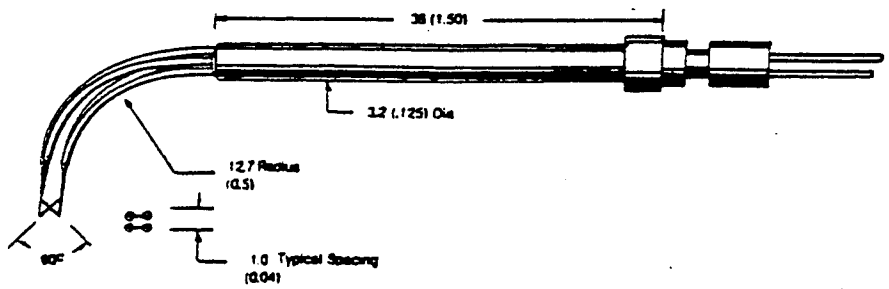

Figure 3.12: x-y or "uv" Probe

Each wire on the probe had a length of 1 mm and a diameter of 51 μm, and had a coefficient of resistance of 0.24%/°C at 20° C. This coefficient was assumed to be constant for the range of temperatures encountered in this study. The probe was placed in a probe holder which was connected to the traverse. The probe holder was connected to the anemometer, which will be discussed in Section 3.5.3, via cables. The resistance of each wire of the probe was then

measured using a four-wire method with a Hewlett-Packard 3468A digital multimeter, and then it was recorded for future use.

3.5.3 Anemometer. As mentioned above the hot-wire probes were connected to the anemometer by cables. The anemometer processed the signal from the hot-wire and sent the signal to the Nicolet for recording. The anemometer used in this study was a constant temperature TSI Inc. IFA 100 System Intelligent Flow Analyzer. It contained a Model 150 anemometer, a model 157 Signal Conditioner, and transducers for each hot-wire channel all of which were housed in a Model 158 master cabinet. The symmetrical bridge used in the IFA 100 had a top resistance of 50 Ω (R_S) and also allowed for an external bridge arm. The external bridge arm was used to set an overheat ratio for each wire of the probe by adding a given resistance to the bridge. An overheat ratio is the ratio between the probe resistance and the resistance on the external bridge arm. The overheat ratio allowed the production of different wire temperatures which are needed for the data reduction. The resistance on the external bridge arm was created by the use of breadboards and resistors. All the external resistances were measured using a four-wire method with a Hewlett-Packard 3468A digital multimeter. The planned range for the overheats was to be 1.3 to 1.95.

In order to ensure the highest frequency response from the cross-wire, the IFA had to be tuned in the supersonic freestream. This was done initially before any testing was started and at any time that the freestream data became noisy. The tuning was accomplished via the IFA 100 and done with the probe in the center of the test section with the injector off. The tuning involved

sending a test square wave signal through the cross-wire probe and then using an oscilloscope to tune the probe's response to this signal.

In addition to the tuning, a calibration run had to be performed for each overheat used. These calibration runs consisted of placing the probe in the center of the test section with the injector off, turning on the tunnel and the wire channels, and then varying the tunnel total pressure from approximately 10 kPa to 285 kPa. This data was recorded using the Nicolet. Through the data reduction described in the Appendix, approximately seven to ten points were taken from these calibration runs to produce the linear regression calibration constants a and b in Equation (4.10).

Multiple overheats were used in this study. During data runs, the cross-wire data was acquired at the center line of the flow at a station 72 throat widths downstream of the injection. Multiple overheat cross-wire anemometry requires at least three overheat ratios to solve for the turbulence intensities and correlations. To obtain accurate turbulence results with the multiple overheat cross-wire anemometry, six overheat ratios were used. This is more than the required three and allowed for a least squares analysis to be applied to the data. The desired overheat ratios ranged from 1.3 to 1.95. The actual overheat value depended on the resistance available from the external arm of the IFA 100 bridge, the breadboards. The actual overheat ratios are tabulated in Table 3.4.

Table 3.4: Actual Overheat Ratios used for Multiple Overheat Data

	"uv" Probe	
Overheat	Wire 1	Wire 2
1	1.92	1.95
2	1.83	1.79
3	1.66	1.70
4	1.61	1.62
5	1.44	1.40
6	1.35	1.32

A data run was performed for each overheat ratios during which the injector was opened and the probe was traversed through the mixing layer. All the data channels shown in Table 3.2 were recorded by the Nicolet during these runs.

3.6 Computational Facilities

This section briefly describes the computational facilities used during this study. As mentioned earlier, the traverse was run by a Compaq 386 computer. All the data that was recorded by Nicolet was displayed real-time on a Zenith 486 computer using windows software provided with the Nicolet system. The data was also saved to the hard drive of the computer. The data reduction portion of this study was performed on the Zenith 486 computer and on AFIT's Sun Sparc 20 work stations. A detail description of the procedure used to reduce this data is given in the Appendix A. The two-dimensional plots seen in this study were produced using Grapher for windows.

IV. Data Reduction Techniques

This chapter presents the techniques used for data reduction during this study. The techniques used to reduce the mean flow will be discussed first, followed by those for the cross-wire.

4.1 Mean Flow

Two different types of data were acquired for the mean flow. The first type was the upstream total conditions, $P_{t\infty}$ and $T_{t\infty}$. The other type of data collected was downstream profiles of Pitot pressure (P_{t2}) and cone-static pressure (P_C). The ratio of the cone-static pressure to the Pitot pressure is typically a function of the Mach number. This function comes from the solution of axisymmetric flow over a cone. The function for a 10° cone was least-squares fit by Bowersox[5], and is given by

$$\frac{1}{M} = -0.052976 + 4.6840x - 18.6786x^2 + 50.7006x^3 - 54.1577x^4 \qquad (4.1)$$

where $x = p_C/p_{t2}$. This equation is valid for Mach numbers between 1.5 and 4.4 and has a standard deviation of 0.06%. With the Mach number and the local total temperature (discussed below) known, the typical compressible flow equations for thermally and calorically perfect gases were used to compute additional flow properites (ρ, u, v, and p).

4.2 Cross-wire

The methods used to reduce the cross-wire data is considerably more difficult than those of the mean flow (Section 4.1). The techniques used to reduce the cross-wire anemometry data collected during this study are discussed in this section.

4.2.1 General Theory. For turbulent compressible flow, the Nusselt number of a cylinder (i.e. hot-film probe) has the following functional form.[15]

$$Nu = f(L / d, M, Pr, Re_e, \tau) \tag{4.2}$$

In this functional relationship, L/d is the wire aspect ratio, M is the Mach number, Pr is the Prandtl number, Re_e is the effective cooling Reynolds number based on the wire diameter, and τ is the temperature loading factor [$\tau = (T_w - T_e)/T_t$], where T_w is the wire temperature and T_e is the temperature the unheated wire would attain if placed in the flow, called the equilibrium temperature. Equation (4.2) reduces to

$$Nu = f(Re_e, \tau) \tag{4.3}$$

for flows where the Mach number normal to the wire is greater then approximately 1.2, the Prandtl number is a constant, the Reynolds number is greater than about 20, and the wire aspect ratio > 1.[15] For wires that are

normal to the flow, experimental hot-wire data has been found to collapse onto the following curve.

$$Nu = (a\sqrt{Re} + b) \tag{4.4}$$

Using equation (4.4) requires that the hot-wire be calibrated at each wire temperature.

The Nusselt number is defined here as

$$Nu = \frac{q_w}{\pi k_t L(T_w - T_e)} \tag{4.5}$$

where $q_w = i_w^2 R_w$ (the wire heat transfer = the wire power) and from anemometer circuit analysis $i_w = V_w/(R_w + R_s + R_L)$ (i_w = the wire current, R_w= the wire resistance, and V_w = wire voltage). Note that for $Re > 20$, $T_e \approx 97\%$ of T_t. Thus T_e is assumed to be T_t in both the calibration process and the data reduction process. With this, the Nusselt number can be expressed as

$$Nu = \frac{V_w^2 R_w}{(R_w + R_s + R_L)^2} \frac{1}{\pi k_t L(T_w - T_t)} \tag{4.6}$$

To derive the hot-wire fluctuation equation, it must be first noted that

$$\frac{\overline{V_w}^2}{C_o} = \left(\frac{\overline{T_t}}{T_o}\right)^{n_k} \left[a\sqrt{\overline{Re_e}} + b\right]\left(T_w - \overline{T_t}\right) \tag{4.7}$$

where

$$C_o = \frac{(R_w + R_s + R_L)^2}{R_w} \pi l k_o \qquad (4.8)$$

and $n_k = 0.89$. Then the wire voltage, the effective Reynolds number, and the total temperature must be replaced by their mean and fluctuating components, the binomial theorem must be applied, and only first order term retained. Solving for $v'_w/\overline{V}_w$ results in the hot-wire fluctuation equation given below.

$$\frac{v'_w}{\overline{V}_w} = f\left(\frac{Reo'_e}{\overline{Reo}_e}\right) + g\left(\frac{T'_t}{\overline{T}_t}\right) \qquad (4.9)$$

In this equation f and g are the hot-wire sensitivities, and are given by

$$f = \frac{1}{4}\left(1 + \frac{b}{a\sqrt{\overline{Re}_e}}\right)^{-1} \text{ and } g = \frac{-\overline{T}_t}{2(T_w - \overline{T}_t)} + \frac{n_k}{2} - fn_\mu \qquad (4.10)$$

In order to determine the hot wire sensitivities, f and g, the mean quantities $\sqrt{\overline{Re}_e}$ and $\overline{T}_t$ must be known. In order to do this, Equation (4.7) can be rewritten as

$$\sqrt{\overline{Re}_e} + x_i \overline{T}_t \sqrt{\overline{Re}_e} + y_i \overline{T}_t = z_i \qquad (4.11)$$

where $x_i = -1/T_{wi}$, $y_i = -b_i/(a_i T_{wi})$, and $z_i = \overline{V}^2_{wi}/(C_i a_i T_{wi}) - b_i/a_i$. In Equation (4.11) C is C_o with k_o replaced with k_t and i is the overheat number. A minimum of two overheat ratios are necessary to determine the two

unknowns, $\overline{\sqrt{Re_e}}$ and $\overline{T}_t$. If more than two overheat ratios are used, then a least squares analysis yields

$$N\overline{\sqrt{Re_e}} + \overline{T}_t\left(\sum y_i - \sum x_i z_i\right) + 2\overline{T}_t\overline{\sqrt{Re_e}}\sum x_i + \overline{T}_t^{\,2}\sum x_i y_i + \overline{T}_t^{\,2}\overline{\sqrt{Re_e}}\sum x_i^2 = \sum z_i \tag{4.12}$$

$$\overline{\sqrt{Re_e}}\left(\sum y_i - \sum x_i z_i\right) + \overline{T}_t\sum y_i^2 + 2\overline{\sqrt{Re_e}}\,\overline{T}_t\sum x_i y_i + \overline{\sqrt{Re_e}}^{\,2}\sum x_i + \overline{\sqrt{Re_e}}^{\,2}\overline{T}_t\sum x_i^2 = \sum y_i z_i \tag{4.13}$$

where N is the number of overheat ratios, and the summations are over the i overheat ratios. The above system was solved numerically using a secant method.

Equation (4.9) was squared and averaged to obtain the turbulence results. This yields the following equation.

$$f_i^2\overline{\left(\frac{Reo_e'}{Reo_e}\right)^2} + 2f_i g_i\overline{\left(\frac{Reo_e'}{Reo_e}\frac{T_t'}{T_t}\right)} + g_i^2\overline{\left(\frac{T_t'}{T_t}\right)^2} = \overline{\left(\frac{v_w'}{V_w}\right)_i^2} \tag{4.14}$$

To resolve the turbulence terms, three overheat ratios are required. If more than three are used then a least squares analysis can be used. The General Least Squares Method (GLS-Method) can be derived if a least squares analysis is used on Equation (4.14). This produces the following 3x3 system

$$\begin{bmatrix} \sum f_i^4 & \sum f_i^3 g_i & \sum f_i^2 g_i^2 \\ \sum f_i^3 g_i & \sum f_i^2 g_i^2 & \sum f_i g_i^3 \\ \sum f_i^2 g_i^2 & \sum f_i g_i^3 & \sum g_i^4 \end{bmatrix} \begin{pmatrix} \overline{\left(\frac{Reo_e'}{Reo_e}\right)^2} \\ \overline{\left(\frac{Reo_e'}{Reo_e}\frac{T_t'}{T_t}\right)} \\ \overline{\left(\frac{T_t'}{T_t}\right)^2} \end{pmatrix} = \begin{pmatrix} \sum f_i^2 \overline{\left(\frac{v_w'}{V_w}\right)_i^2} \\ \sum f_i g_i \overline{\left(\frac{v_w'}{V_w}\right)_i^2} \\ \sum g_i^2 \overline{\left(\frac{v_w'}{V_w}\right)_i^2} \end{pmatrix} \tag{4.15}$$

where the summations are over the N overheat ratios and i denotes the overheat number. The next step in the data reduction process it to specify Re_e for the cross-wire probe used to collect the data.

4.2.2 Cross-Wire. The use of a cross-wire (or swept wire) in supersonic flow has not received a great deal of attention. Early work published by NACA in the 1950's found that the cross-wire response was independent of Mach number if $M \sin\phi \geq 1$.[16] Thus Equation (4.3) is valid for this study.

The following equations are derived in tunnel coordinates, where the angle ϕ, is defined as the angle between the axis and the normal to the wire with positive being counter-clockwise. The transformation matrix shown below gives the relationship between the normal and tangential Reynolds number components to the x and y components.

$$\begin{pmatrix} Re_n \\ Re_t \end{pmatrix} = \begin{bmatrix} \cos(\phi) & \sin(\phi) \\ -\sin(\phi) & \cos(\phi) \end{bmatrix} \begin{pmatrix} Re_x \\ Re_y \end{pmatrix} \tag{4.16}$$

The functional form of Re_e that is going to be used in Equation (4.4) is given by

$$\begin{aligned} Re_e^2 &= Re_n^2 \\ &= A_1 Re_x^2 + 2A_2 Re_x Re_y + A_3 Re_y^2 \end{aligned} \tag{4.17}$$

where A_i are given by the following.

$$\begin{aligned} A_1 &= \cos^2(\phi) \\ A_2 &= \cos(\phi)\sin(\phi) \\ A_3 &= \sin^2(\phi) \end{aligned} \tag{4.18}$$

If Reo_e, Reo_x, and Reo_y, are replaced by their mean plus fluctuating component, the Binomial Theorem is used, and the following definitions are used,

$$\begin{aligned} R_o &= \frac{\overline{Reo_y}}{\overline{Reo_x}} \\ B_1 &= \frac{A_1}{B_3} \\ B_2 &= \frac{A_2}{B_3} \\ B_3 &= A_1 + 2A_2 R_o \end{aligned} \tag{4.19}$$

it can be shown that

$$\begin{aligned} \overline{Reo_{ej}} &= \overline{Reo_x}\sqrt{B_{3j}} \\ \left(\frac{\overline{Reo_e'}}{\overline{Reo_e}}\right)_j &= B_{1j}\left(\frac{\overline{Reo_x'}}{\overline{Reo_x}}\right) + B_{2j}\left(\frac{\overline{Reo_y'}}{\overline{Reo_x}}\right) \end{aligned} \tag{4.20}$$

where j indexes one of the two wires on the cross-wire probe. This derivation assumes that $R_o^2 \ll 1$. From this equation the cross-wire response equation can be obtained, and the methods of Section 4.2.1 can be applied to the two wire on the cross-wire probe.

The mean results can be resolved into the x and y components of Re by using the mean equation in Equation (4.20) and the results from both wires. By solving Equation (4.20) the following can be shown.

$$\overline{Reo_x}^2 = \frac{\overline{Reo_{e1}}^2 / A_{21} - \overline{Reo_{e2}}^2 / A_{22}}{A_{11}/A_{21} - A_{12}/A_{22}} \tag{4.21}$$

$$\overline{Reo_y} = \frac{1}{2\overline{Reo_x}} \frac{\overline{Reo_{e1}}^2 / A_{11} - \overline{Reo_{e2}}^2 / A_{12}}{A_{21}/A_{11} - A_{22}/A_{12}}$$

The turbulence results can be also be resolved into x and y components by using the fluctuation equation in Equation (4.20), yielding.

$$\overline{\left(\frac{Reo_x'}{Reo_x}\right)^2} = \frac{1}{D_2^2}\left[\frac{1}{B_{21}^2}\overline{\left(\frac{Reo_e'}{Reo_e}\right)_1^2} - \frac{2}{B_{21}B_{22}}\overline{\left(\frac{Reo_e'}{Reo_e}\right)_1\left(\frac{Reo_e'}{Reo_e}\right)_2} + \frac{1}{B_{22}^2}\overline{\left(\frac{Reo_e'}{Reo_e}\right)_2^2}\right]$$

$$\overline{\left(\frac{Reo_y'}{Reo_x}\right)^2} = \frac{1}{D_1^2}\left[\frac{1}{B_{11}^2}\overline{\left(\frac{Reo_e'}{Reo_e}\right)_1^2} - \frac{2}{B_{11}B_{12}}\overline{\left(\frac{Reo_e'}{Reo_e}\right)_1\left(\frac{Reo_e'}{Reo_e}\right)_2} + \frac{1}{B_{12}^2}\overline{\left(\frac{Reo_e'}{Reo_e}\right)_2^2}\right]$$

$$\overline{\left(\frac{Reo_x'}{Reo_x}\frac{Reo_y'}{Reo_x}\right)} = \frac{1}{2B_{11}B_{21}}\left[\overline{\left(\frac{Reo_e'}{Reo_e}\right)_1^2} - B_{11}^2\overline{\left(\frac{Reo_x'}{Reo_x}\right)^2} - B_{21}^2\overline{\left(\frac{Reo_y'}{Reo_x}\right)^2}\right] \tag{4.22}$$

where $D_1 = (B_{21}/B_{11} - B_{22}/B_{12})$ and $D_2 = (B_{11}/B_{21} - B_{12}/B_{22})$. The GLS-Method can be used to solve for all the terms on the right hand side of Equation (4.22) except for the middle correlation between wire 1 and wire 2. This term can be

found from the covariance between the two wires on the cross-wire probe. The relationship for the covariance is given below.

$$\overline{\left(\frac{v'_w}{V_w}\right)_1\left(\frac{v'_w}{V_w}\right)_2} = f_1 f_2 \overline{\left(\frac{Reo'_e}{Reo_e}\right)_1\left(\frac{Reo'_e}{Reo_e}\right)_2} + g_1 g_2 \overline{\left(\frac{T'_t}{T_t}\right)} + f_1 g_2 \overline{\left(\frac{Reo'_e}{Reo_e}\frac{T'_t}{T_t}\right)_1} + f_2 g_1 \overline{\left(\frac{Reo'_e}{Reo_e}\frac{T'_t}{T_t}\right)_2} \tag{4.23}$$

The fluctuation x and y components of the Reynolds number can now be computed with the use of Equation (4.23).

The Reynolds number total temperature correlations are the remaining turbulence variables that need to be decomposed into x and y components. It can be shown that

$$\overline{\frac{Reo'_x T'_t}{Reo_x T_t}} = \frac{1}{D_2}\left[\frac{1}{B_{21}}\overline{\left(\frac{Reo'_e}{Reo_e}\frac{T'_t}{T_t}\right)_1} - \frac{1}{B_{22}}\overline{\left(\frac{Reo'_e}{Reo_e}\frac{T'_t}{T_t}\right)_2}\right]$$

$$\overline{\frac{Reo'_y T'_t}{Reo_x T_t}} = \frac{1}{D_1}\left[\frac{1}{B_{11}}\overline{\left(\frac{Reo'_e}{Reo_e}\frac{T'_t}{T_t}\right)_1} - \frac{1}{B_{12}}\overline{\left(\frac{Reo'_e}{Reo_e}\frac{T'_t}{T_t}\right)_2}\right] \tag{4.24}$$

4.2.3 Separation of Turbulence Variables. Multiple overheat cross-wire anemometry in supersonic flow provides the following "conservative" variable turbulence data.

$$\overline{(\rho u_i)'(\rho u_j)'} \quad \overline{T_t'^2} \quad \overline{(\rho u_i)' T'_t} \tag{4.25}$$

Two assumptions are made in order to separate the "conserved" turbulence data into the "non-conservative" variables. The first assumption is a thermally perfect gas ($p=\rho RT$). The second assumption is that the effects pressure fluctuations on the hot-wire response equations are small compared to the density and temperature fluctuations. The following results can be obtained by making first order assumptions. The p' terms are included for completeness.

$$\frac{u'}{\bar{u}} = \frac{(\rho u)'}{\overline{\rho u}} - \frac{\rho'}{\bar{\rho}}$$

$$\frac{v'}{\bar{u}} = \frac{(\rho v)'}{\overline{\rho u}} - R_o \frac{\rho'}{\bar{\rho}} \qquad (4.26)$$

$$\frac{\rho'}{\bar{\rho}} = \frac{1}{\alpha+\beta}\left[\beta\left(\frac{(\rho u)'}{\overline{\rho u}}\right) - \frac{T_t'}{\bar{T}_t} + \alpha\frac{p'}{\bar{p}}\right]$$

In these equations, $\alpha = [1 + 0.5(\gamma-1)M^2]^{-1}$ and $\beta = (\gamma-1)\alpha M^2$. Using Equation (4.26) and assuming p' = 0, then all the turbulent shear terms in the "Reynolds Averaged" Navier-Stokes equations can be obtained. The assumption that $p' \approx 0$ is a controversial one. Kistler[17] suggested that p' is on the order of u'^2, which is second order and can be neglected. The effects of p' can be seen in the density fluctuation equation in Equation (4.26). It should also be noted that the p' term is multiplied by a factor of α, which is always less than 1. Thus, even if p' is not equal to zero, the effects on separating the hot-wire variables may still be small. The validity of the $p' \approx 0$ assumption has been experimentally verified for a Mach 4.0 free mixing layer.[9]

In order to obtain the terms in the "Favre Averaged" Navier-Stokes equations, the following relationships are used

$$\frac{\overline{u''}}{U} = -\frac{\overline{\rho' u'}}{\overline{\rho u}}$$

$$\frac{\overline{v''}}{U} = -\frac{\overline{\rho' v'}}{\overline{\rho u}} \qquad (4.27)$$

$$\overline{u''v''} = \overline{u'v'}$$

where ( )" correspond to Favre (mass) averaged fluctuating components, and $U = \overline{\rho u}/\overline{\rho}$.

V. Results

This chapter presents the results of the normal slot injection compressible turbulence data acquisition and reduction. The nominal freestream wind tunnel conditions were determined to be $M_\infty = 2.9$, $P_{t\infty} = 203 \pm 3$ kPa, and $T_{t\infty} = 298 \pm 3$ K. Shadowgraph and schlieren photographs were taken of the entire flowfield. Mean flow and multiple overheat cross-wire data was taken at the measuring position downstream 72 throat diameters along the centerline of the flow.

5.1 Flow Two Dimensionality and Repeatibility

Two concerns that were brought up in the development stages of this experiment, was whether or not the flow would be two dimensional and how repeatable would the flow conditions be.

To determine how two dimensional the flow really was, Pitot and cone static measurements were taken at two axial stations. One station was upstream of the measurement station (x/W = 32) and one was downstream of the measurement stattion (x/W = 82). At theses two stations measurements were made at 7 spanwise locations and from -2.20 to 2.20 cm in the transverse directions. The data from the two probes was reduced to produce two Mach number contour plots. These plots are shown in Figures 5.1 and 5.2. These contour plots show that the flowfield is mostly two dimensional. Some three dimensionality, as expected due to the boundary layer on the side walls, is seen near the wall but does not effect the centerline flow, the point of this study's measurements. Thus this flow field can be considered two dimensional.

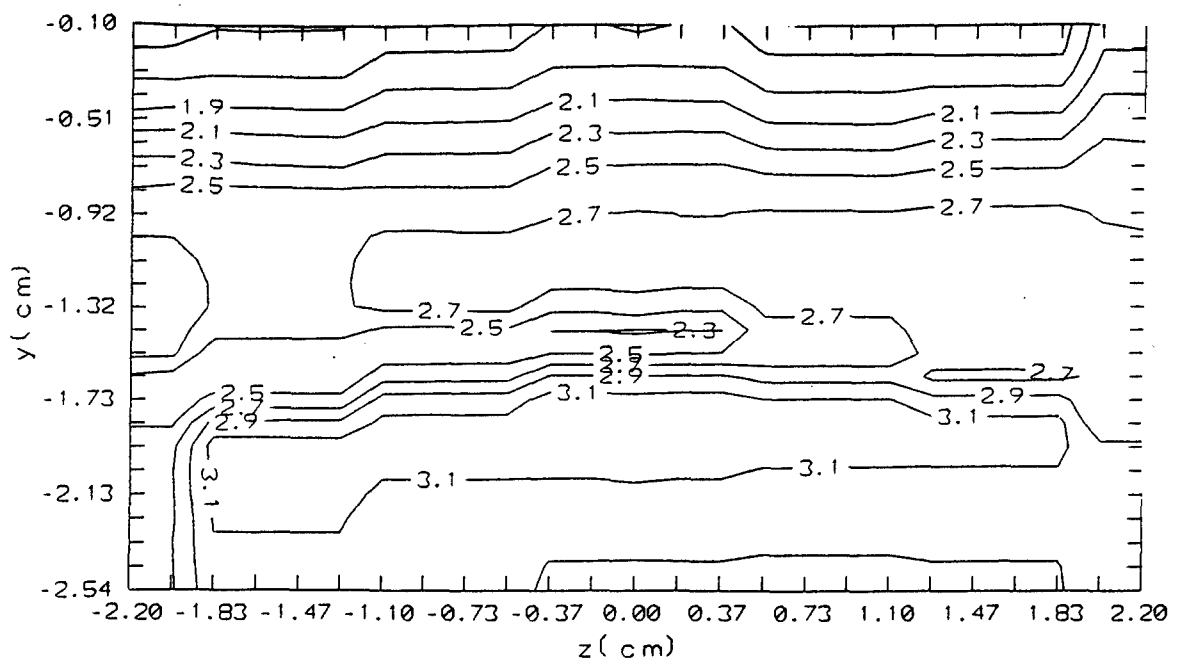

Figure 5.1: Upstream Mach Number Contours

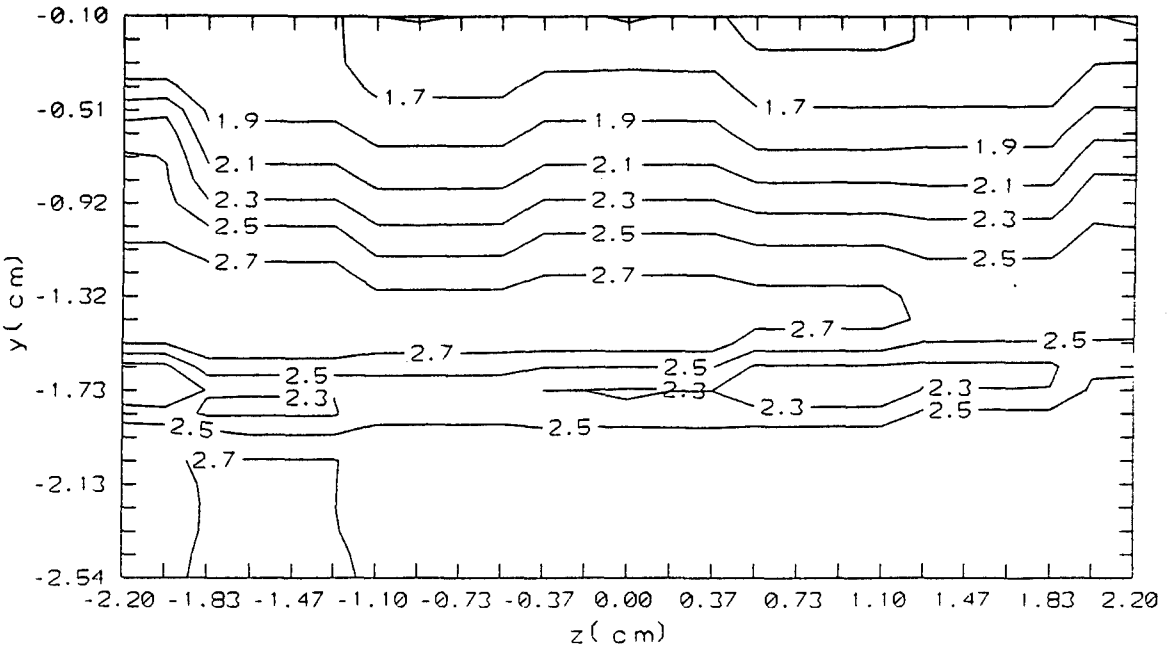

Figure 5.2: Downstream Mach Number Contours

These contour plots also show flow repeatibility since the different spanwise measurements were taken during different runs of the tunnel and show good agree in the plots. Another statement of repeatibility is shown in Figure 5.3. This is a plot of the cross-wire shear for this study and a companion study of heated and cooled injection. In this figure, the adiabatic case, this study, splits the heated and cooled cases as expected. That in itself is a good indication of valid data, but the fact that the data needed for this result was taken during many runs of the tunnel and over 5 months of testing shows that the flowfield conditions were very repeatable.

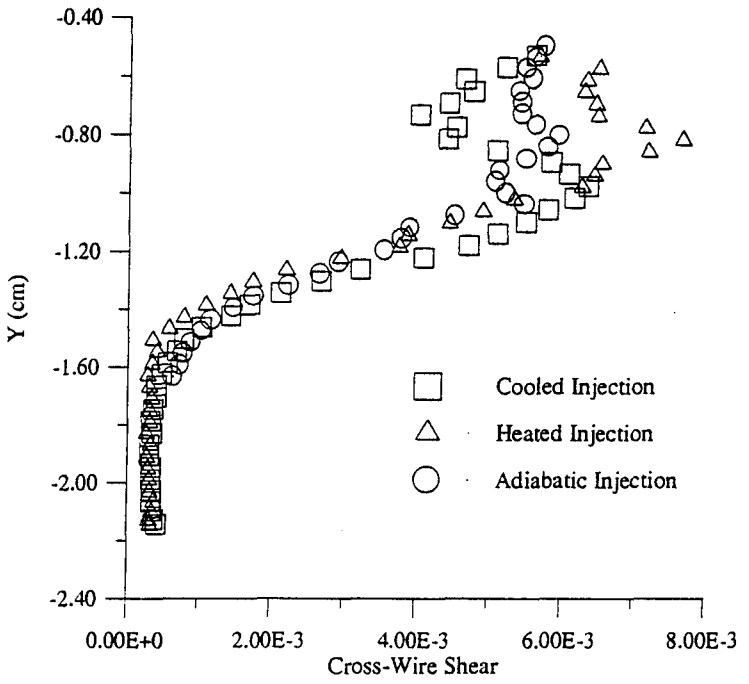

Figure 5.3: Comparison of Cross-Wire Shear with the Cross-Wire Shear of a Companion Study

5.2 *Shadowgraph and Schlieren Analysis*

The photographs produced by the shadowgraph and schlieren flow visualization techniques provided great insight into the nature of the flowfield being studied. The shadowgraph of the flowfield is shown in Figure 5.4, and the schlieren is shown in Figure 5.5.

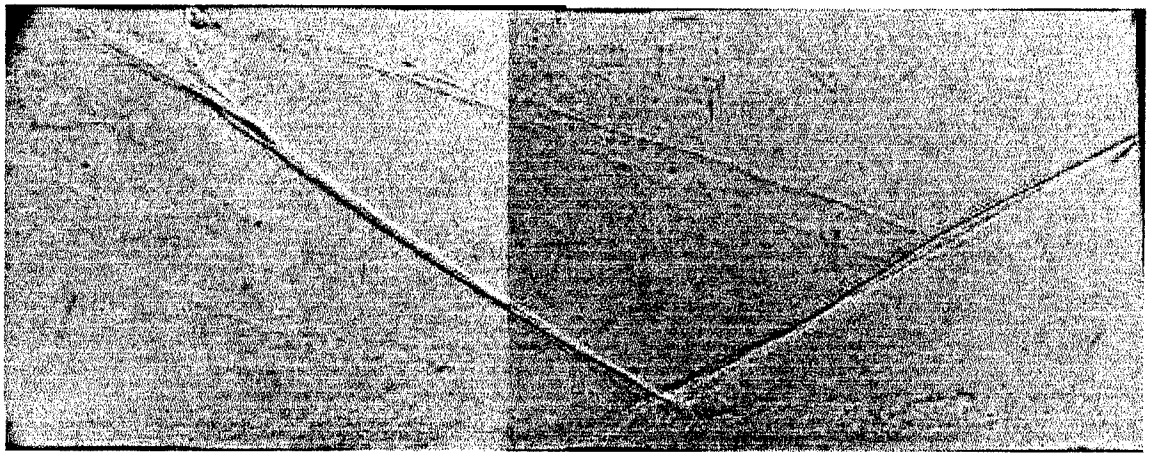

Figure 5.4: Shadowgraph Flow Visualization of the Entire Flowfield

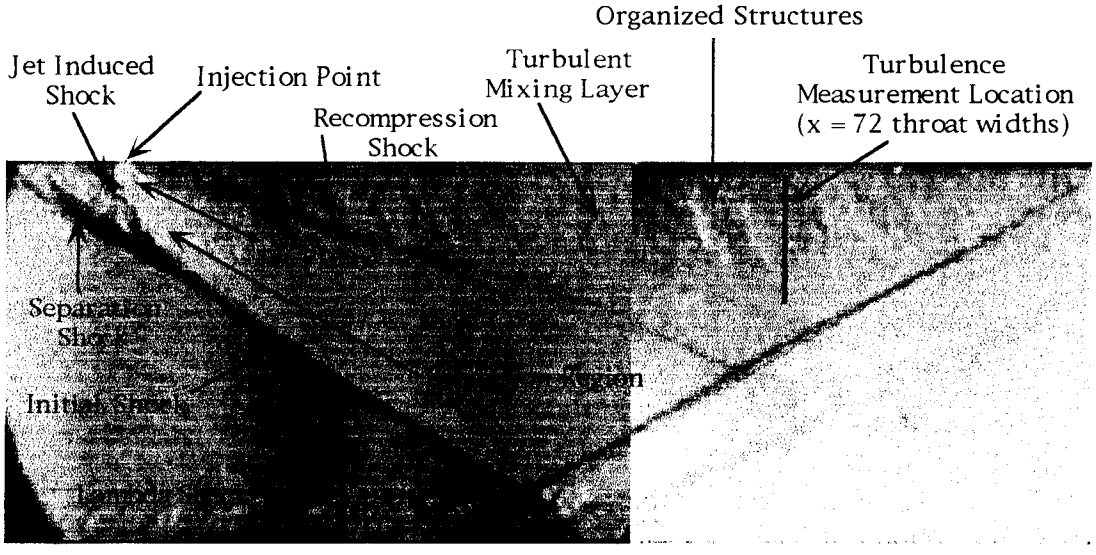

Figure 5.5: Schlieren Flow Visualization with Major Flow Components

These photographs show the major components of the flowfield. These include the separation shock, the recompression shock, the Mach disk in the jet plume , the jet induced shock, the lambda shock on the lower surface, and of course the turbulent mixing layer. The separation shock is caused by the separation of the boundary layer due to the injector plume. This shock combines with the jet induced shock wave which is caused by the jet plume itself to form the initial shock wave. Though not completely clear in the photographs, the supersonic jet plume is terminated by a normal shock. This is known as a Mach disc. The recompression shock is formed when the boundary layer reattaches and flows parallel to the wall. As the jet flow is turned into the cross-flow direction, an expansion is created. The lighter region between the initial shock and the recompression shock provides conclusive evidence of this expansion. The lambda shock on the lower surface is caused by the initial shock interacting with the lower boundary layer and causing it to separate. The separated flow then causes a shock wave to form ahead of it, thus forming the lambda shape. Lastly the turbulent mixing layer is caused by the interaction of the injected flow with the freestream flow. Organized structures are clearly present in the mixing layer. All of the features mentioned above are pointed out in Figure 5.5.

Since the goal of this research was to investigate the turbulent flow structure, measurements were resricted to a single axial location. The location of the conventional and cross-wire probes measurement station was based on these photographs. It was chosen to be at x = 72 throat widths which translates to 11.43 cm from the injection point. This location was chosen to allow for the thickest mixing layer while not encountering any shock waves in the mixing layer or the freestream immediately after the mixing layer.

5.3 Conventional Probes

The conventional probe data consisted of Pitot and cone-static profiles taken at the measurement station. These profiles where then used to construct a Mach number profile. This profile is shown in Figure 5.6. Every ten points of collected data was averaged together to create this profile.

The mixing layer can be easily seen in this profile. The local edge Mach number ($M_e \approx 2.7$) was slightly lower than the freestream value of approximately 2.9. The losses through the two shock waves are responsible for the reduction. The region between y = 0 cm and y = 1.5 cm contains the boundary layer and the turbulent mixing layer in which the Mach number vary from approximately 1.4 to about 2.7 at the edge of the mixing layer. Even though the flow was fully turbulent, as will be described below, the Mach number profile across the mixing layer resembled that of a laminar boundary layer. The unsteadiness of the turbulent mixing layer can be seen in the fluctuations of the Mach profile near the edge of the mixing layer. These fluctuations might have been caused by the mixing layer edge moving as the probe was traversing that area of the flow. Figure 5.7 is a plot of static pressure non-dimensionalized by the freestream total pressure. As seen from the figure, this remained constant throughout the mixing layer and into the freestream. The mean flow data collected had an additional purpose other than providing insight into the mean characteristics of the flow. It was needed as an input for the cross-wire data reduction.

5.4 Cross-Wire Probe

An x-y or "uv" type cross-wire probe was used to collect data at the measurement station for six overheats. The data from these six overheats were processed using the procedure described in the Appendix to generate Figures 5.8 through 5.27. In several of the plots, the values are shown normalized by the local freestream values. The local freestream properties are shown in Table 5.1 below.

Table 5.1: Local Freestream Values for Several Flow Properties

Local Freestream Property	Value	Error
Mass Flux (rhou bar)	118 kg/m^2s	± 3 kg/m^2s
Mass Flux (rho bar u bar)	133 kg/m^2s	± 4 kg/m^2s
Density	0.224 kg/m^3	± 0.0045 kg/m^3
Velocity	592 m/s	± 4 m/s
Total Temperature	293 K	± 4 K
Reynolds Number	333	± 14.5

Figure 5.8 shows the mass flux flow angle This angle is between 2 and 3 degrees with the larger angles in the turbulent mixing layer. Since this flow was of the "thin layer" type, the flow angle should have been small. The slight angle could be from probe misalignment.

Figure 5.9 shows the mean mass flux profiles and as expected the axial component is the largest and drops off in the mixing layer due to the decreasing local Mach number. Figure 5.10 shows the mass flux profile which drops off in the mixing layer. This result was generated with Mach number and the total temperature profile from the x-wire. Figure 5.11 shows a

comparison between the two mass flux measurements. The agreement between the two is good except close to the wall.

Figures 5.12 and 5.13 show the mean flow density the mean flow respectively. The mean density decreases in the mixing layer. The axial velocity is greater than the transverse velocity, and it drops off across the mixing layer. In general, the results obtained with the x-wire agreed well with those from the mean flow probes.

Figure 5.14 shows the total temperature profile. Since this injection was adiabatic, this quantity should have been fairly constant. As can be seen, the total temperature only varies by 2%. Do to the strong interaction and large turbulent shear, it was expected that some of the freestream kinetic energy would be dissipated into heat in this region which could account for the 2% increase in total temperature. Figure 5.15 shows how the Reynolds number drops off within the mixing layer as expected when the density and velocity both drop off in the same region.

Figures 5.16 and 5.17 show the mass flux and separated turbulence intensity profiles respectively. From Figure 5.16, it can be seen that the transverse mass flux turbulent intensity is about 50% of the axial value. Also from this figure, the total temperature fluctuation is about 6%, which is higher than expected for this approximately adiabatic flow. The dissipation of kinetic energy as described above was most likely responsible for this. In Figure 5.17, the axial and transverse velocity fluctuations are almost of the same magnitude. The transverse velocity fluctuation is about 90% of the axial fluctuation. This result was expected since the wall damping found in boundary layer studies was minimal here. On the other hand, the density fluctuation peeks at 5% at the edge of the mixing layer and then decreases.

The increase in the density fluctuation near the edge of the mixing layer can be explained. Freestream and injector kinetic energy is being converted into thermal energy at the interface between the freetream and the mixing layer through shearing. The increase in thermal energy causes higher static temperature fluctuations near the boundary between the freesteam and the mixing layer. Since density fluctuations are strongly dependent on the static temperature fluctuations, higher density fluctuations should be expected near the mixing layer-freestream interface. The velocity fluctuations are not affected as much by temperature, thus there is not great increase in the velocity fluctuations through the mixing layer. These two phenomena are clearly depicted in Figure 5.17.

Figures 5.18 and 5.19 display the mass flux total temperature correlations and the compressible heat flux data. In both sets of data the axial term is larger than the transverse term. In the case of the mass flux total temperature correlations the transverse term is only 66% of the axial term. And for the compressible heat flux data, the transverse term is only 50% of the axial term. Even though the transverse terms are smaller than the axial terms, they are not zero, and for thin layer type flows these are the important terms that require modeling.

Figures 5.20 and 5.21 present the velocity-velocity and density-velocity correlations respectively. These results will be used to estimate the Reynolds shear stresses. Figure 5.22 shows the compressible turbulent kinetic energy (TKE), and figure 5.23 shows the incompressible turbulent kinetic energy. The graphs show that the incompressible TKE is only 67% of the compressible TKE.

Figure 5.24 presents estimates of the Reynolds shear stress. The circles in this graph represent the incompressible term, while the squares represent

the first compressible term. The triangles represent the second compressible term and the "X"'s represent the total Reynolds shear [see Equation (2.12)]. From the graph, it can be seen that the incompressible term is 3 times larger than the compressible term. This means that for this particular situation compressibility accounts for 25% of the total level of Reynolds shear.

Figure 5.25 present the cross-wire terms in the transformed form of the turbulent shear stress. The first term in this transformed representation can be directly measured by the cross-wire. From Figure 5.25 it can be seen that this term is the dominate term of the transformed cross-shear. Therefore, the cross-wire measures taken can be assumed to accuately depict the turbulent shear.

Finally for completeness, Figures 5.26 and 5.27 present the Favre (or mass averaged) data. The Favre shear shown in figure 5.27 has the same magnitude as the incompressible Reynolds shear term.

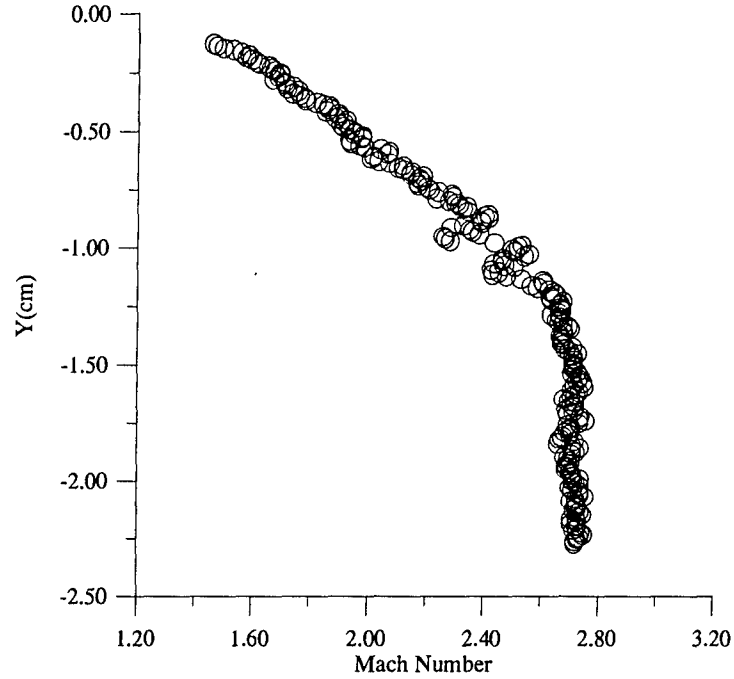

Figure 5.6: Mach Number Profile from Conventional Probes

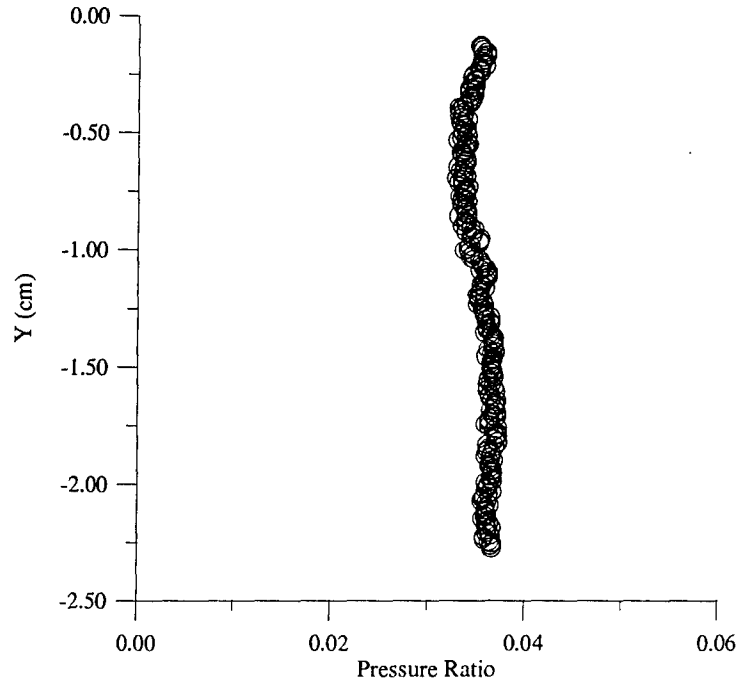

Figure 5.7: Static Pressure Non-Dimensionalized by Freestream Total Pressure

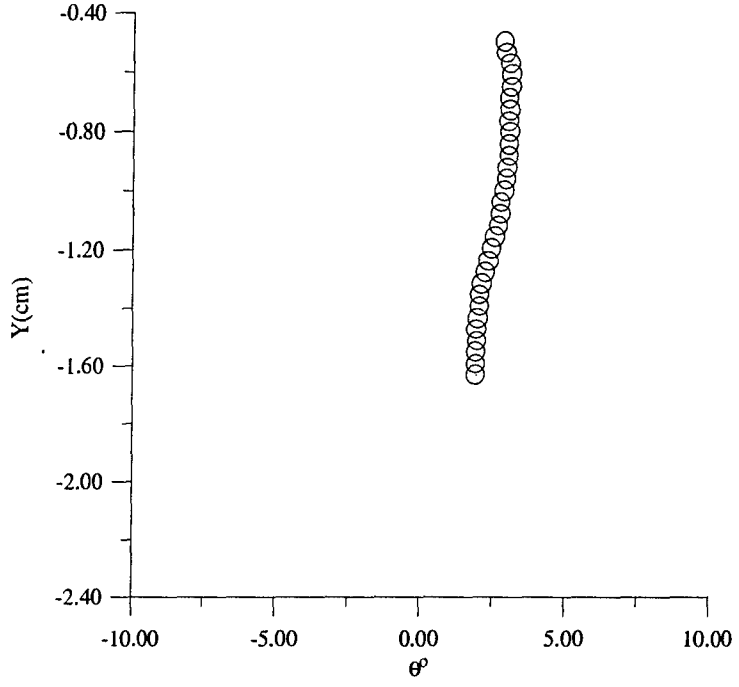

Figure 5.8: Mass Flux Flow Angle

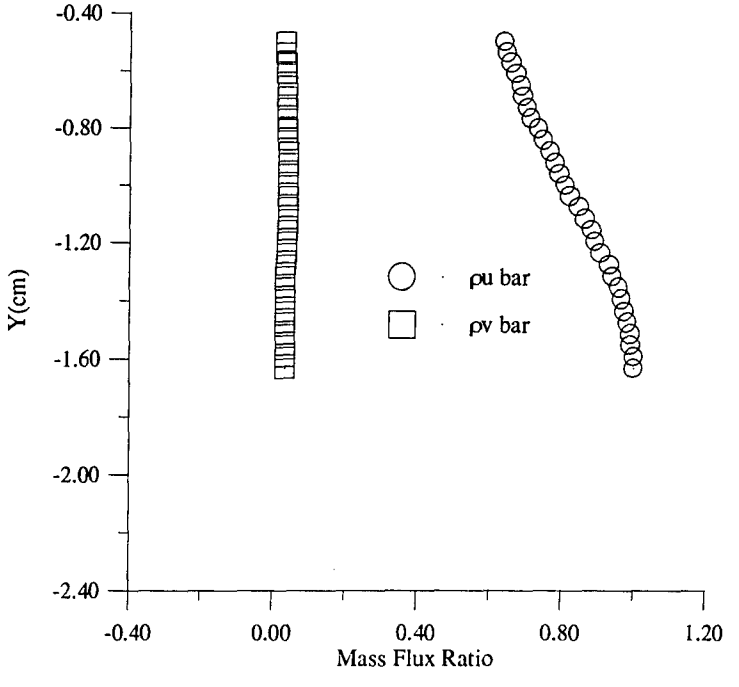

Figure 5.9: Mass Flux Non-Dimensionalized by the Freestream Condition

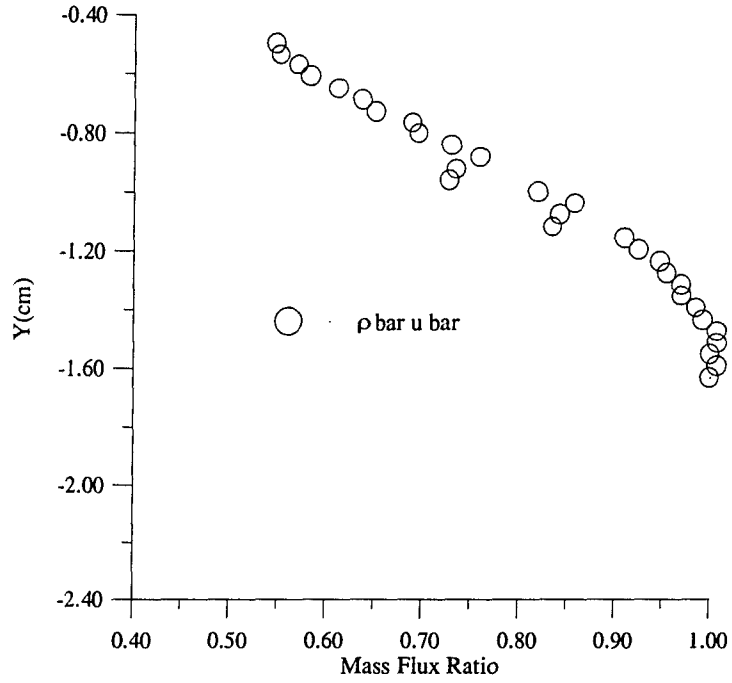

Figure 5.10: Mass Flux Non-Dimensionalized by the Freestream Condition

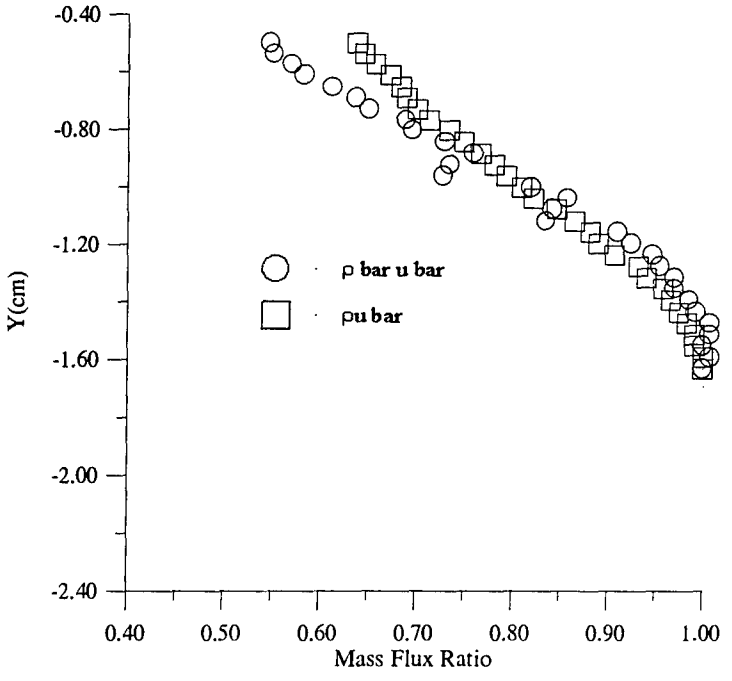

Figure 5.11: Comparison of the Two Mass Flux Measurements

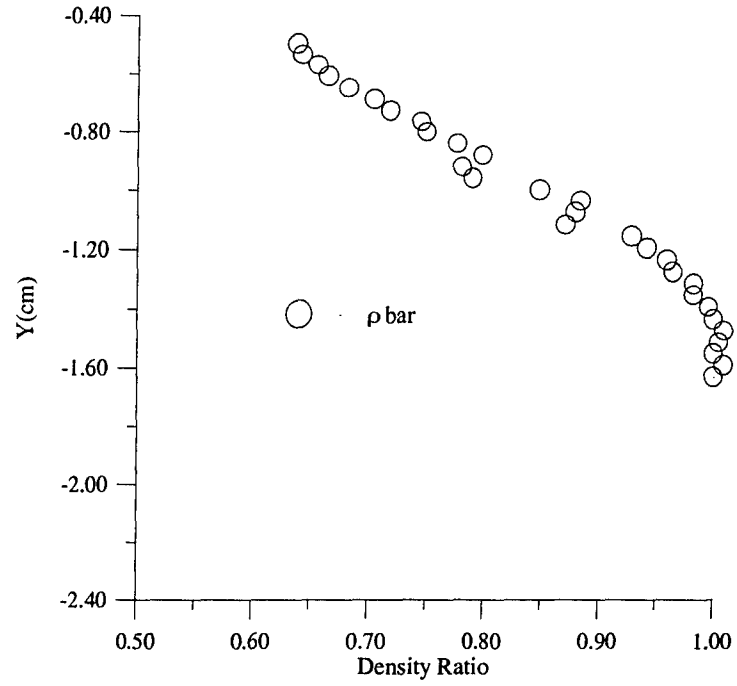

Figure 5.12: Measured Averaged Density

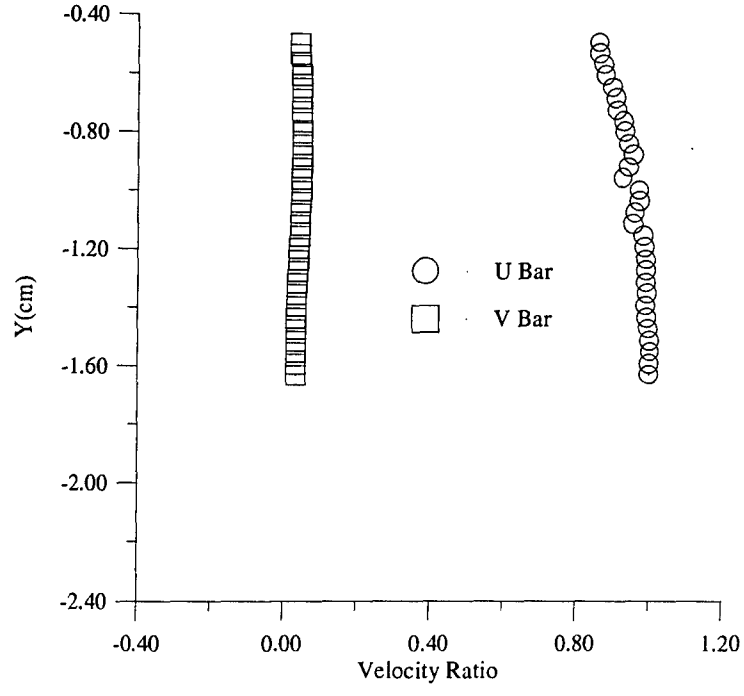

Figure 5.13: Mean Flow Velocity Non-Dimensionalized by the Freestream Condition

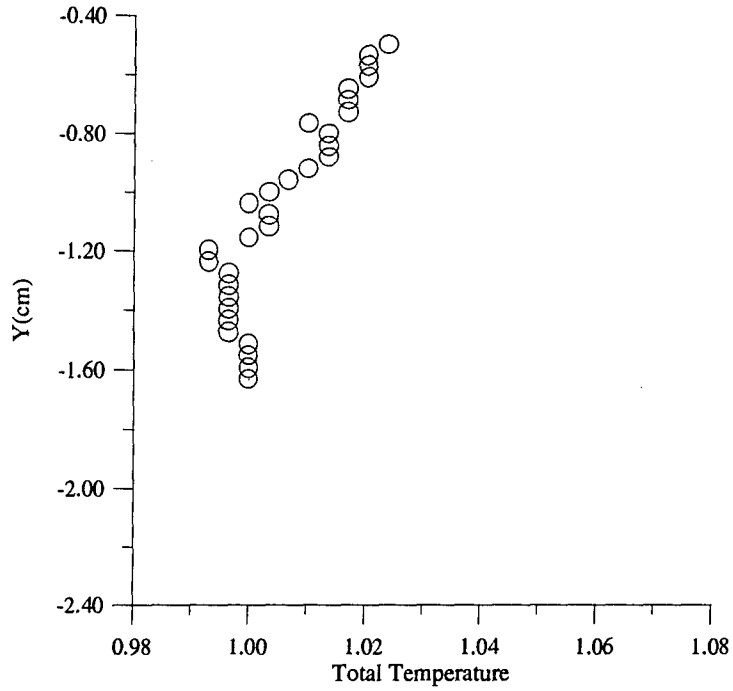

Figure 5.14: Total Temperature Non-Dimensionalized by the Freestream Condition

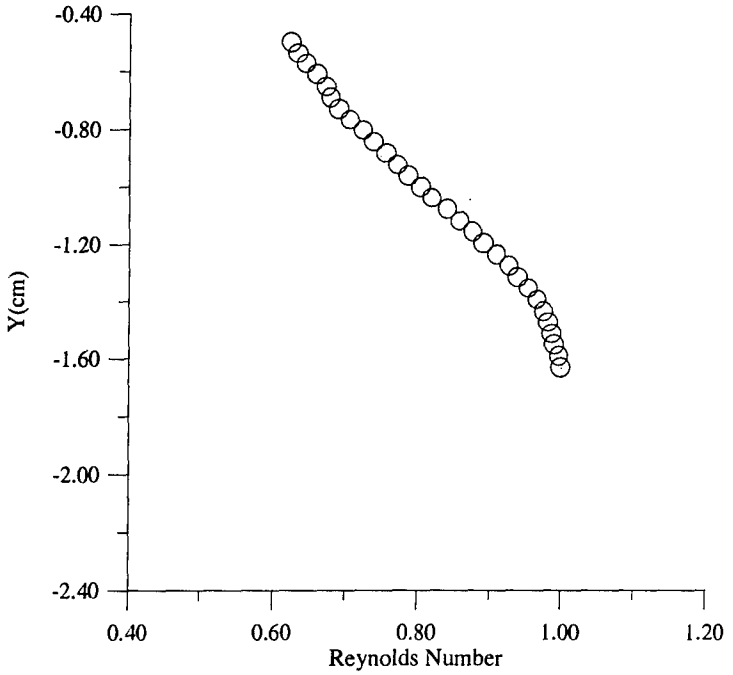

Figure 5.15: Reynolds Number Non-Dimensionalized by the Freestream Condition

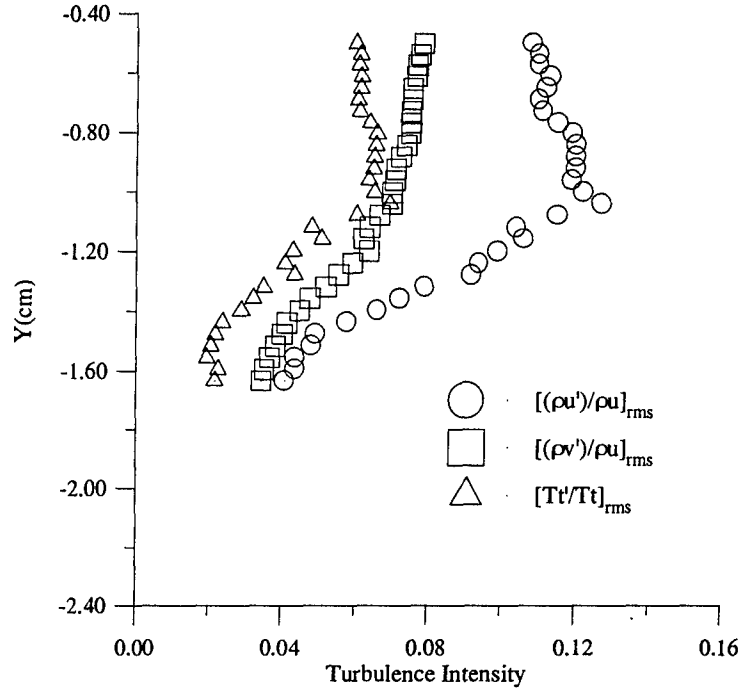

Figure 5.16: Adiabatic Injection Turbulence Intensities

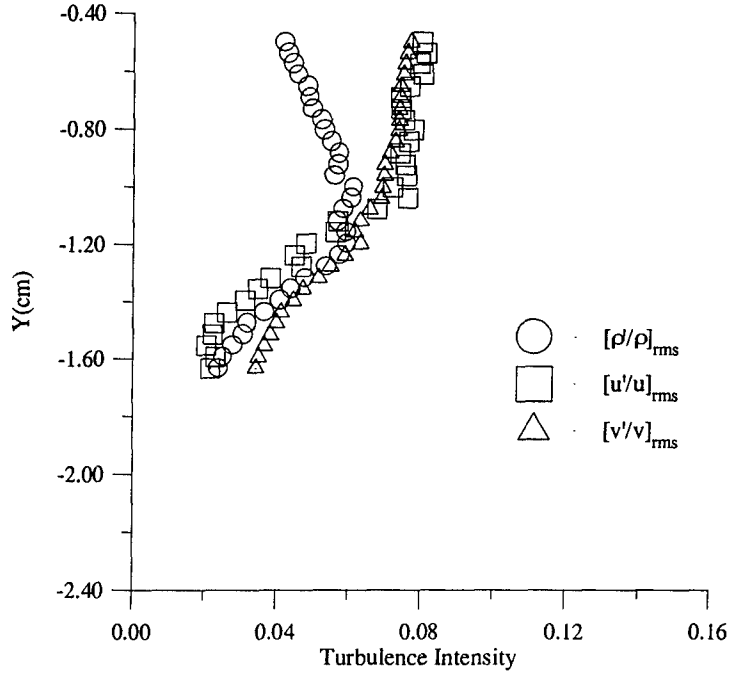

Figure 5.17: Adiabatic Injection Separated Turbulence Intensities

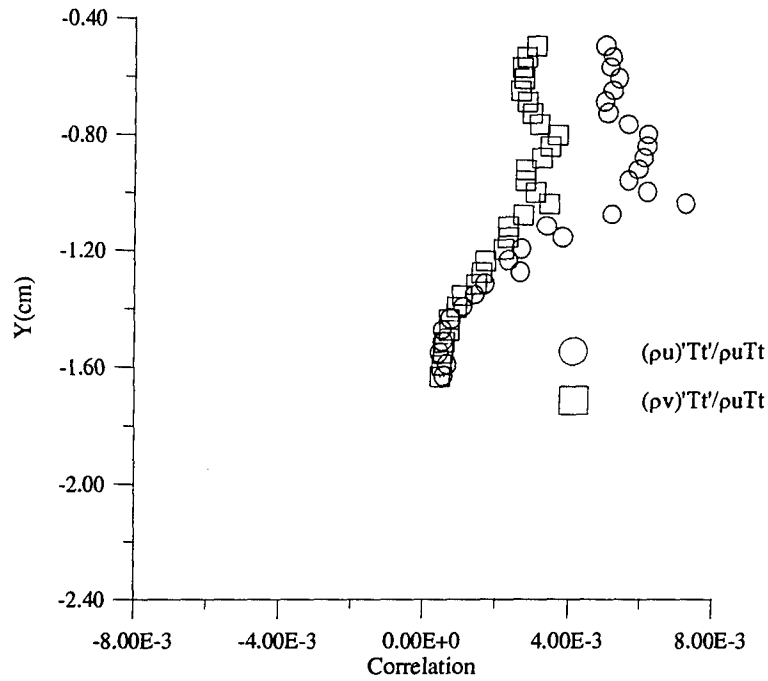

Figure 5.18: Adiabatic Injection Mass Flux-Total Temperature Fluctuation Correlations

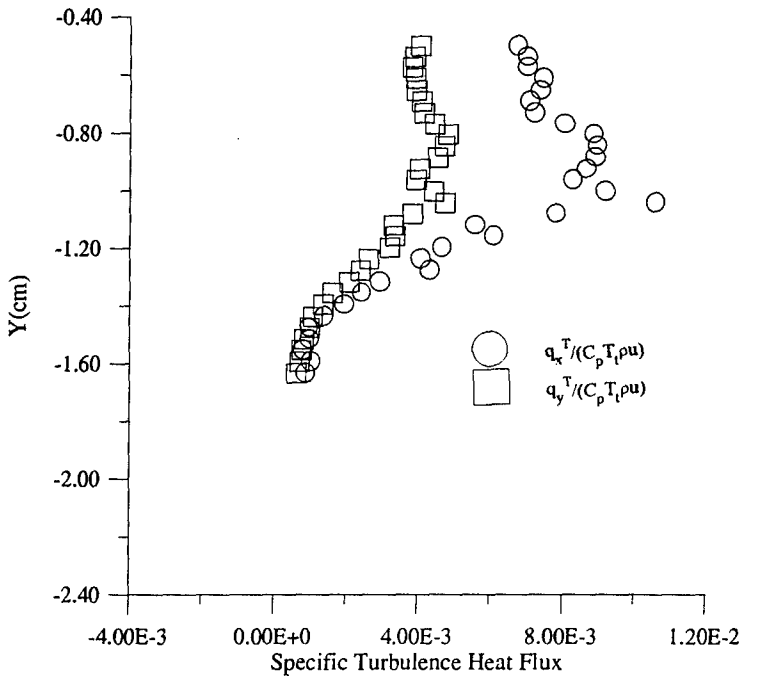

Figure 5.19: Adiabatic Specific Turbulence Heat Flux

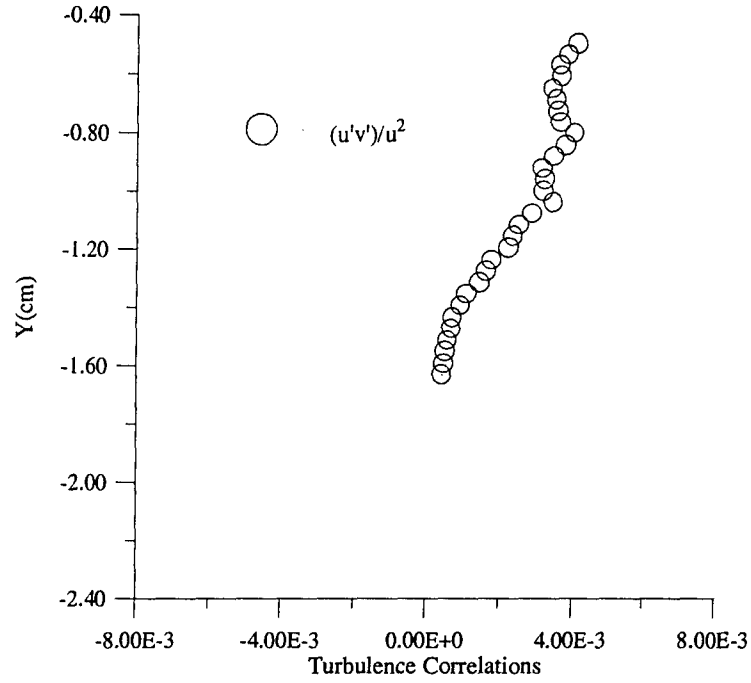

Figure 5.20: Adiabatic Injection Velocity-Velocity Correlation

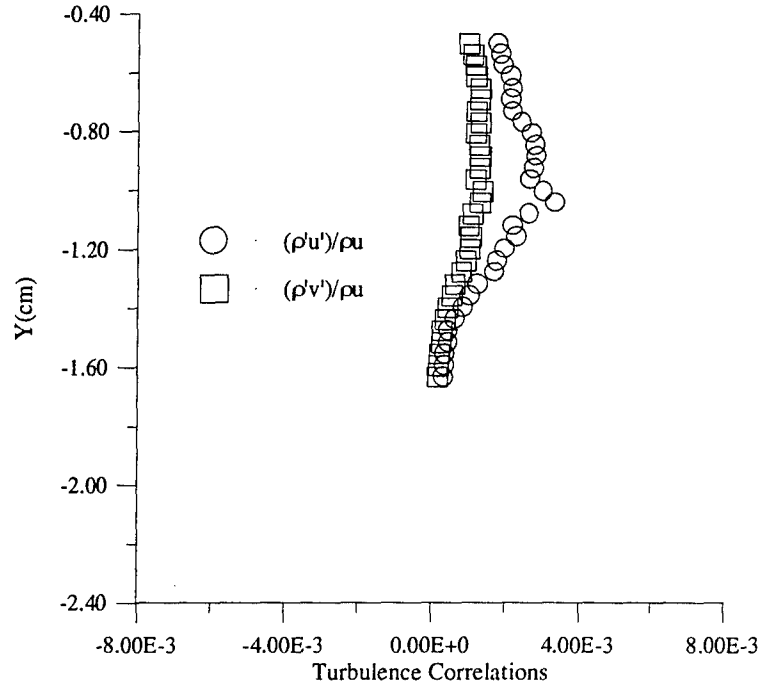

Figure 5.21: Adiabatic Injection Velocity-Density Correlations

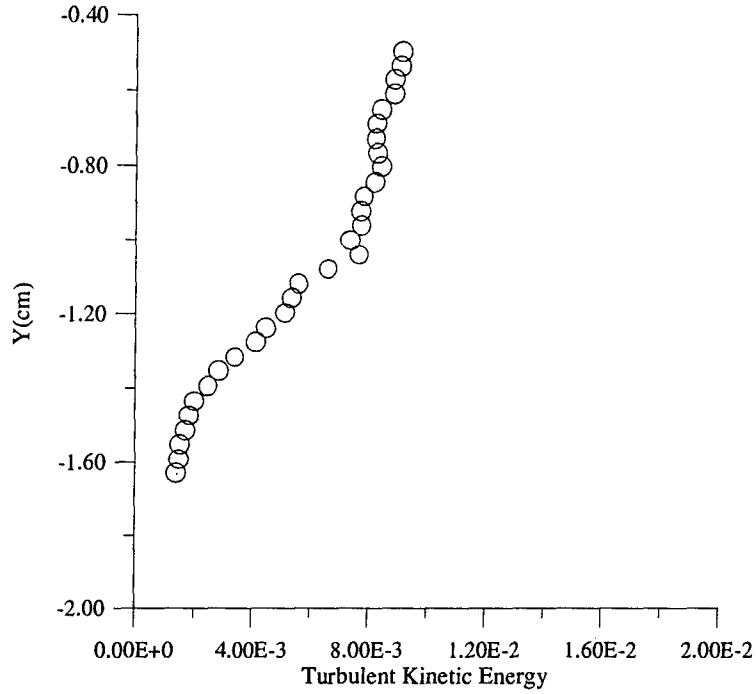

Figure 5.22: Incompressible Turbulent Kinetic Energy

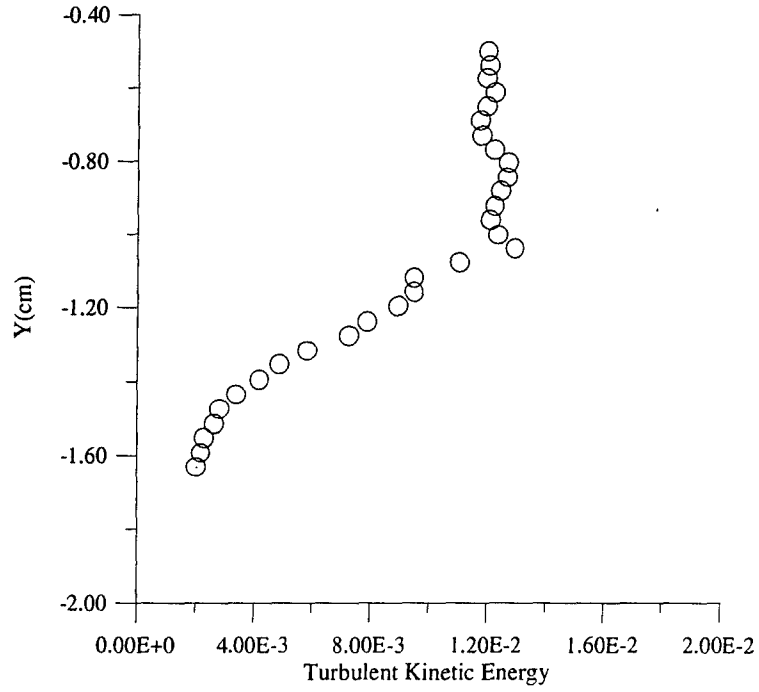

Figure 5.23: Compressible Turbulent Kinetic Energy

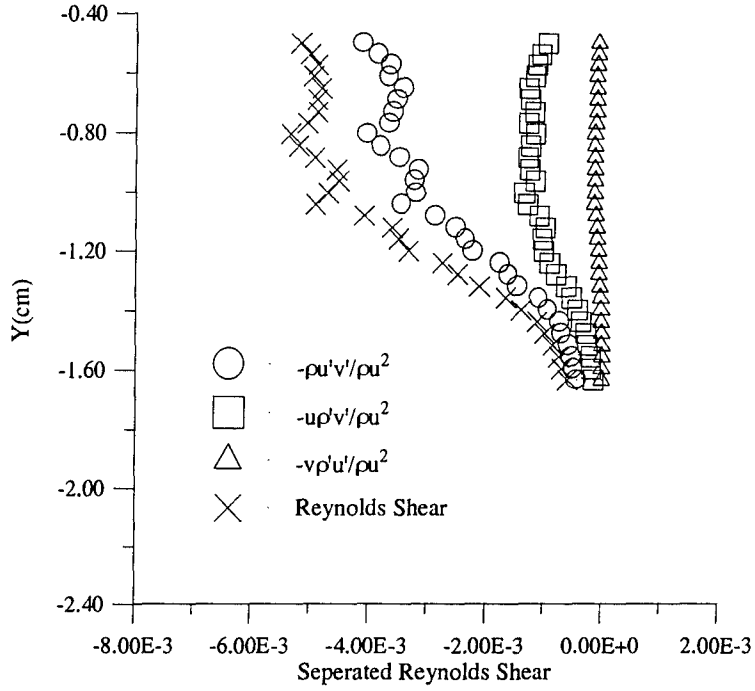

Figure 5.24: Separated Reynolds Shear Terms

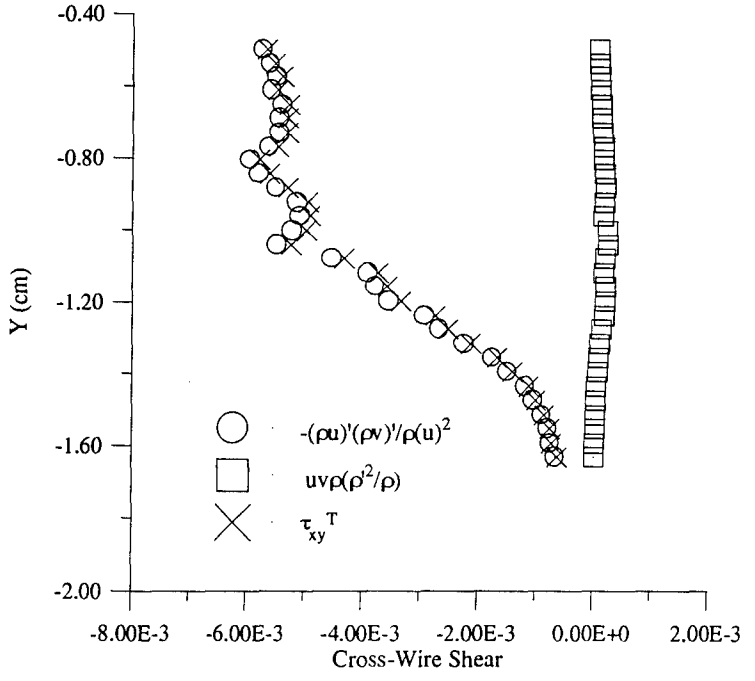

Figure 5.25: Cross-Wire Shear Terms

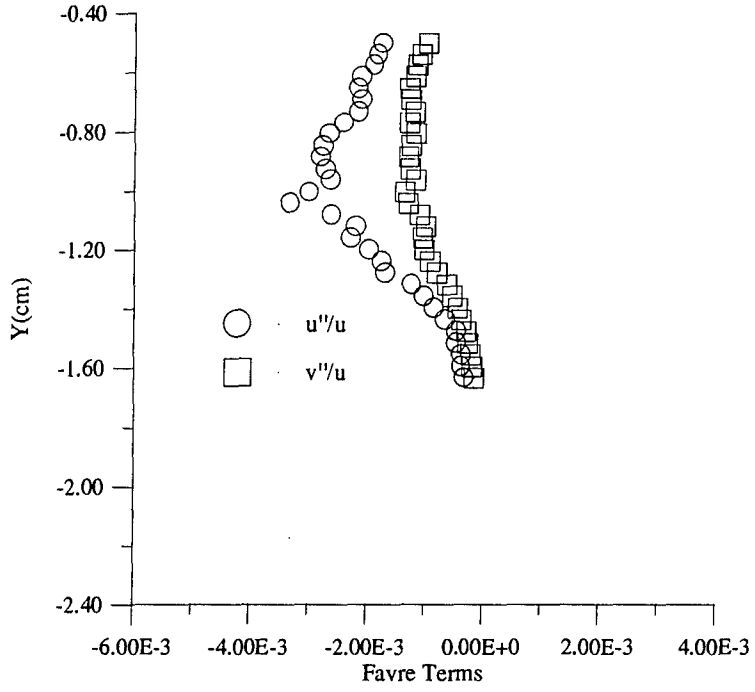

Figure 5.26: Adiabatic Injection Favre Terms

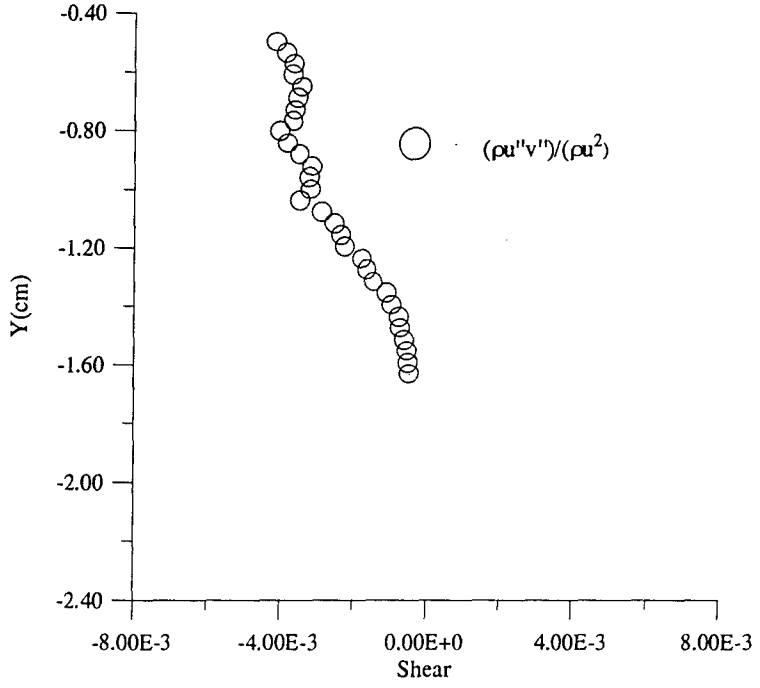

Figure 5.27: Adiabatic Injection Favre Shear

VI. Conclusions and Discussion

6.1 Conclusions

An experimental investigation of the mean and turbulent flowfield associated with Mach 1.6 normal injection into a Mach 2.9 cross flow was performed. The mean flow data and the flow visualizations gave an insight into the overall flow structure and guided the choice of an appropriate measuring location for turbulence data.

It was determined from the multiple overheat hot-wire anemometry data that the incompressible shear stress term dominated the flow field. It accounted for up to 75% of the total Reynolds shear stress. The axial compressible term was smaller than the incompressible term, but it was still relatively large. It made up almost the remaining 25% of the total Reynolds shear stress, thus models ignoring this term could still prove to be inadequate when it comes to modeling compressible flow turbulence. Secondly, the extremely violent interaction within the flowfield has an effect on the flow properties near the interface between the mixing layer and the freestream. The fluctuations in the density increased in this region. This is believed to be do to the conversion of the freestream's and possibly the jet's kinetic energy into thermal energy at the interface by the way of shearing. This effect was also noticeable in the total temperature fluctuations which were higher than expected in the mixing layer at 6%, and in the new total temperature which increased 2% in the mixing layer.

6.2 Recommendations for Further Study

Based on other turbulent mixing layer studies, compressible effects manifest themselves by making the compressible shear term of the total Reynolds shear stress the largest term. The fact that this expected compressibility effects did not show up in the results of this study, suggests that further investigation of this particular flowfield is necessary to fully understand the nature of the flow. This could be done in a number of ways. First, this particular experiment could be expanded to include both x-y and x-z probes to ensure that the data correlates between the probes.

Another suggestion is to acquire data at more axial measurement locations to provide insight into the turbulent flow development.

Lastly, using alternative investigative techniques, such as a triple hot-wire probe or Laser Doppler Velocimetry (LDV) may lead to a greater understanding of the flow structure.

Appendix A

A.1 Cross-Wire Data Reduction Procedure

This section briefly describes the procedure for reducing the data received from the hot-wire . The first step was to take the files that were saved during the data collection and convert them form wave form files to readable text files. This was accomplished by a software application that came with the Nicolet. Once the data files were converted into a readable form, they were processed by a FORTRAN program written by this author. This program averaged every 4096 points in the hot-wire channel files. Running this program produced seven files for each overheat. These files are a mean voltage value for each wire on the probe (.bar files), a voltage rms value for each wire on the probe (.rms files), a file that contains seven to ten points based on the averaged calibration file data for each wire on the probe (.cal files), and a correlation file (.cor file) between the two wires. The program also produce the Mach number profile based on the Pitot and cone-static data collected.

Once these files were produced, they were ready to be feed in to the Multiple Overheat Supersonic Hot-Wire Anemometry Reduction Program (MSHeAR). This is a computer program written by Dr. Bowersox to reduce just such data. The first step when using MSHeAR is to give it the overheat information and wire information. This is done via an input file or deck and is created with MSHeAR. Next the deck must be read into the program . Third, the wires are calibrated using the .cal files and MSHeAR. Forth, the wire data was reduced using the General Least Squares (GLS method). This produced an

output file that contained the cross-wire results (Section 4.2.2). This is usually run through a recursive filter to eliminate some of the scatter associated with experimental data. Then the filtered data was run through the separation of variables routine (Section 4.2.3) in order to produce the separated Reynolds shear stresses and other separated flow parameters. This data was then plotted as seen in Section 5.3.

Appendix B

B.1 Error Analysis Computations

Scatter, or error, is a natural part of taking any measurement, particularly when measuring an unknown quantity. This section presents the results of an error analysis performed. The method used in this study was the L_2 (or Euclidean)[18] norm as the measure of the error. The L_2 norm is given by

$$e_x = \left[\sum_{i=1}^{n} e_i^2 \right]^{1/2} \tag{5.1}$$

where i indexes the various errors associated with the measurement if x.

B.1.1 Conventional Probes

The error associated with the conventional probes comes from the calibration errors associated with the pressure transducers. The error associated with the pressure transducers used in this study was taken to be 0.25% based on the manufactures standards. From this the error associated with the Mach number was determined to be 2%. Based on this value and reference [22], the errors in Table B.1 were associated with the mean flow values.

Table B.1: Mean Flow Errors

Quantity	Error
e_M	2%
e_{Tt}	2.7%
e_u	1.3%
$e_{p/PTt}$	3%
$e_{Pt/Pt1}$	11%
e_ρ	4%
$e_{\rho u}$	5.3%

B.1.2 Cross-wire Probe

The errors found in the conventional probes carried over into the calculations for the cross-wire probe errors. Using reference [22] again, the cross-wire probe errors were determined. The results are listed below in Table B.2.

Table B.2: Cross-Wire Errors

Quantity	Error
$e_{\rho u}$	5.82%
e_f	2.9%
$e_{Reo}{}^2$	5.82%
$e_{Rex}{}^2$	17.4%
e_{Rex}	8.7%
$e_{u"/u}$	22%
$e_{\tau xy}{}^T/_{\rho u}{}^2$	20%

Bibliography

1. Rizzetta, D. P., "Numerical Simulation of Slot Injection into a Turbulent Supersonic Stream," *AIAA Journal*, Vol. 30, No. 10, October 1992.

2. Anderson, D.A., Tannehill, J. C., and Pletcher, R. H., *Computational Fluid Mechanics and Heat Transfer*, McGraw-Hill, New York, 1984.

3. Settles, G. S., and Dobson, L. J., "Supersonic and Hypersonic Shock/ Boundary-Layer Interaction Database," *AIAA Journal*, Vol. 32, No. 7, July 1994.

4. Liou, W. W., and Shih, T. H., "Oh the Basic Equations for the Second-Order Modeling of Compressible Turbulence," NASA TM 105277, October 1991.

5. Bowersox, R. D. W., "Compressible Turbulence in a High-Speed High-Reynolds Number Mixing Layer," PhD Dissertation, Virginia Polytechnic Institute and State University, VA, Department of Aerospace Engineering, September 1992.

6. Tucker, Kelly C.., "Experimental Investigation of Non-Adiabatic Supersonic Slot Injection into a Supersonic Cross-Flow," MS Thesis, AFIT/GAE/ENY/95D, School of Engineering, Air Force Institute of Technology (AU), Wright-Patterson AFB OH, December 1995.

7. Shapiro, A. H., *The Dynamics and Thermodynamics of Compressible Flow, Volume II*, Krieger Publishing Company, Malabar, Florida, 1954.

8. Wilcox, D. C., *Turbulent Modeling for CFD*, DCW Inc., La Canada, CA, 1993.

9. Bowersox, R. D. W., and Schetz, J. A., "Compressible Turbulence Measurements in a High-Speed High-Reynolds Number Mixing Layer," *AIAA Journal*, Vol. 32, No. 4, pp. 758-764, April 1994.

10. McCann, Gregory J., "Compressible Turbulence Measurement in Low-Angle Injection into A Supersonic Flow," MS Thesis, AFIT/GAE/ENY/95M-03, School of Engineering, Air Force Institute of Technology (AU), Wright-Patterson AFB OH, March 1995.

11. *Nicolet Systems Operation*, Nicolet, Madison, WI, 1991.

12. Huffman, Jr., R. E, "Mach 2.9 Investigation into the Flow Structure in the Vicinity of a Wrap-Around Fin," MS Thesis, AFIT/GAE/ENY/95D, School of Engineering, Air Force Institute of Technology (AU), Wright-Patterson AFB OH, December 1995.

13. McCann, G. J., and Bowersox, R. D. W., "Experimental Investigation of Supersonic Gaseous Injection into a Supersonic Free Stream," unpublished paper, Air Force Institute of Technology (AU), Wright-Patterson AFB OH.

14. "Hot-Wire/Hot-Film Anemometry," TSI Incorporated, St. Paul, MN, 1988.

15. Kovaszney, L. S. G., "The Hot-Wire Anemometer in Supersonic Flow," *Journal of Aeronautical Science*, Vol 17, 1950, pp. 565-584.

16. Spagenberg, W. G., "Heat-Loss Characteristics of Hot-Wire Anemometers at Various Densities in Tramsonics and Supersonic Flow," NACA TN 3381,1955.

17 Kistler, A., "Fluctuation Measurements in a Supersonic Turbulent Boundary Layer," *Physics of Fluids*, Vol. 2, No. 220, 1959.

18. Burden, R. L., and Faires, J. D., *Numerical Analysis*, 5th Ed., PWS Publishing Company, Boston, 1993.

19. Dotter, J. W., "Compressible Turbulence Measurements in Supersonic Flow with Adverse Pressure Gradient," MS Thesis, AFIT/GAE/ENY/94D-10, School of Engineering, Air Force Institute of Technology (AU), Wright-Patterson AFB OH, December 1994.

20. Bowersox, R. D. W., "MSHeAR User's Manual," Department of Aeronautics, Air Force Institute of Technology (AU), Wright-Patterson AFB OH, 1994.

21. Bowersox, R. D. W., "Thermal Anemometry," *Handbook of Fluid Mechanics and Fluid Machinery*, John Wiley & Sons, sect 15.4.2, December 1995, pp. 15.29-15.40.

22. Bowersox, R. D. W., Hand written notes on random error analysis, Department of Aeronautics, Air Force Institute of Technology (AU), Wright-Patterson AFB OH, 1995.

Vita

Christopher D. Whitcomb [redacted] NY to Duane W. and Barbara J. Whitcomb. He graduated from McDowell High School in Erie, PA in June 1986. From there he went on to study Aerospace Engineering at Syracuse University. He graduated Summa Cum Laude from Syracuse University in May 1990 with a Bachelor of Science in Aerospace Engineering. On December 29, 1990, Christopher married the former Cynthia Sue Biebel. He became part of Air Force Space Command, where he performed duties in satellite command and control at Falcon Air Force Base, Colorado Springs, CO for three years. Christopher began his studies at the Air Force Institute of Technology in May of 1994 and completed his Master's degree in December of 1995.

REPORT DOCUMENTATION PAGE

Form Approved
OMB No. 0704-0188

1. AGENCY USE ONLY *(Leave blank)*	2. REPORT DATE	3. REPORT TYPE AND DATES COVERED
	December 1995	Mater's Thesis

4. TITLE AND SUBTITLE
COMPRESSIBLE TURBULENCE MEASUREMENT IN THE MIXING LAYER OF AN ADIABATIC NORMAL SLOT INJECTION INTO SUPERSONIIC FLOW

5. FUNDING NUMBERS

6. AUTHOR(S)
Christopher Duane Whitcomb, Captain, USAF

7. PERFORMING ORGANIZATION NAME(S) AND ADDRESS(ES)
Air Force Institute of Technology, WPAFB, OH 45433

8. PERFORMING ORGANIZATION REPORT NUMBER
AFIT/GAE/ENY/95D-24

9. SPONSORING/MONITORING AGENCY NAME(S) AND ADDRESS(ES)
Dr. A. Negad, WL/POPT
Dr. T. Chen, Taitech Inc.

10. SPONSORING/MONITORING AGENCY REPORT NUMBER

11. SUPPLEMENTARY NOTES

12a. DISTRIBUTION/AVAILABILITY STATEMENT
Approved forn public release, distribution unlimited

12b. DISTRIBUTION CODE

13. ABSTRACT *(Maximum 200 words)*

In this study mean flow and compressible turbulence measurements were taken at a station x = 72W downstream of the injection, where W is the injector throat width, of an adiabatic 2-D Mach 1.6 normal slot injection into a Mach 2.9 flow. Data were collected using a conventional Pitot probe, a cone-static probe, and multiple overheat cross-wire anemometry. In addition, schlieren and shadowgraph flow visualization was used to investigate the flow tructure at both the injection point and the downstream data collection point. From these measurements, mass flux component turbulence intensities of 8% to 10% were seen. The total temperature fluctuation was shown to be 6%, which was higher than expected for this adiabatic case. It was also determined that the incpmpressible component of the Reynolds shear stress accounted for 75% of the total Reynolds shear stress. Another important observation was that the density fluctuation turbulence intensity peaked near the freestrwam edge of the mixing layer. The turbulent dissipation of kinetic energy was most likely the cause of this peak.

14. SUBJECT TERMS
Supersonic turbulent boudary layers, Reynolds-averaged Navier-Stokes equations, supersonic injection

15. NUMBER OF PAGES
84

16. PRICE CODE

17. SECURITY CLASSIFICATION OF REPORT	18. SECURITY CLASSIFICATION OF THIS PAGE	19. SECURITY CLASSIFICATION OF ABSTRACT	20. LIMITATION OF ABSTRACT
Unclassified	Unclassified	Unclassified	UL